

Chandra X-Ray Observations of the X-Ray Faint Elliptical Galaxy
NGC 4697

Craig L. Sarazin – University of Virginia

Jimmy A. Irwin – University of Michigan

Joel N. Bregman – University of Michigan

Deposited 09/14/2018

Citation of published version:

Sarazin, C., Irwin, J., Bregman, J. (2001): Chandra X-Ray Observations of the X-Ray Faint Elliptical Galaxy NGC 4697. *The Astrophysical Journal*, 555(2). DOI: [10.1086/321618](https://doi.org/10.1086/321618)

CHANDRA X-RAY OBSERVATIONS OF THE X-RAY FAINT ELLIPTICAL GALAXY NGC 4697

CRAIG L. SARAZIN,¹ JIMMY A. IRWIN,^{2,3} AND JOEL N. BREGMAN²

Received 2000 December 28; accepted 2001 April 6

ABSTRACT

A *Chandra* ACIS S3 observation of the X-ray faint elliptical galaxy NGC 4697 resolves much of the X-ray emission (61% of the counts from within one effective radius) into 90 point sources, of which ~ 80 are low-mass X-ray binaries (LMXBs) associated with this galaxy. The dominance of LMXBs indicates that X-ray faint early-type galaxies have lost much of their interstellar gas. On the other hand, a modest portion of the X-ray emission from NGC 4697 is due to hot gas. Of the unresolved emission, it is likely that about half is from fainter unresolved LMXBs, while the other half ($\sim 23\%$ of the total count rate) is from interstellar gas. The X-ray-emitting gas in NGC 4697 has a rather low temperature ($kT = 0.29$ keV). The emission from the gas is very extended, with a much flatter surface brightness profile than the optical light, and has an irregular, L-shaped morphology. The physical state of the hot gas is uncertain; the X-ray luminosity and extended surface brightness are inconsistent with a global supersonic wind, a partial wind, or a global cooling inflow. The gas may be undergoing subsonic inflation, rotationally induced outflow, or ram pressure stripping. X-ray spectra of the resolved sources and diffuse emission show that the soft X-ray spectral component, found in this and other X-ray faint ellipticals with *ROSAT*, is due to interstellar gas. The cumulative LMXB spectrum is well fitted by thermal bremsstrahlung at $kT = 8.1$ keV, without a significant soft component.

NGC 4697 has a central X-ray source with a luminosity of $L_X = 8 \times 10^{38}$ ergs s^{-1} , which may be due to an active galactic nucleus and/or one or more LMXBs. At most, the massive black hole (BH) at the center of this galaxy is radiating at a very small fraction ($\leq 4 \times 10^{-8}$) of its Eddington luminosity.

Three of the resolved sources in NGC 4697 are supersoft sources. In the outer regions of NGC 4697, seven of the LMXBs (about 20%) are coincident with candidate globular clusters, which indicates that globulars have a high probability of containing X-ray binaries compared to the normal stellar population. We suggest that all of the LMXBs may have been formed in globulars. The X-ray to optical luminosity ratio for the LMXBs in NGC 4697 is $L_X(\text{LMXB}, 0.3\text{--}10 \text{ keV})/L_B = 8.1 \times 10^{29} \text{ ergs s}^{-1} L_{B\odot}^{-1}$, which is about 35% higher than the value for the bulge of M31. Other comparisons suggest that there are significant variations (factor of ≥ 2) in the LMXB X-ray-to-optical ratios of early-type galaxies and spiral bulges. The X-ray luminosity function of NGC 4697 is also flatter than that found for the bulge of M31. The X-ray luminosities (0.3–10 keV) of the resolved LMXBs range from $\sim 5 \times 10^{37}$ to $\sim 2.5 \times 10^{39}$ ergs s^{-1} . The luminosity function of the LMXBs has a “knee” at 3.2×10^{38} ergs s^{-1} , which is approximately the Eddington luminosity of a $1.4 M_\odot$ neutron star (NS). This knee appears to be a characteristic feature of the LMXB population of early-type galaxies, and we argue that it separates BH and NS binaries. This characteristic luminosity could be used as a distance estimator. If they are Eddington limited, the brightest LMXBs contain fairly massive accreting BHs. The presence of this large population of NS and massive BH stellar remnants in this elliptical galaxy shows that it (or its progenitors) once contained a large population of massive main-sequence stars.

Subject headings: binaries: close — galaxies: elliptical and lenticular, cD — galaxies: ISM — X-rays: galaxies — X-rays: ISM — X-rays: stars

On-line material: machine-readable tables

1. INTRODUCTION

X-ray observations, starting with the *Einstein* X-Ray Observatory, have shown that elliptical and S0 galaxies are luminous sources of X-ray emission (e.g., Forman, Jones, & Tucker 1985). At least for the X-ray luminous early-type galaxies (defined as those having a relatively high ratio of X-ray to optical luminosity L_X/L_B), it is clear that the bulk of the X-ray luminosity is from hot ($\sim 10^7$ K) interstellar gas (e.g., Forman et al. 1985; Trinchieri, Fabbiano, & Canizares 1986). Presumably, the material comprising the interstellar

medium (ISM) originated from stellar mass loss in the galaxy. There is a strong correlation between the X-ray and blue luminosities of early-type galaxies $L_X \propto L_B^{1.7-3.0}$ (Canizares, Fabbiano, & Trinchieri 1987; White & Davis 1997; Brown & Bregman 1998). However, there is a large dispersion in the X-ray luminosities of early-type galaxies of a given optical luminosity. Two galaxies with similar blue luminosities might have X-ray luminosities that differ by as much as a factor of 100 (Canizares et al. 1987; Fabbiano, Kim, & Trinchieri 1992; Brown & Bregman 1998). We will refer to galaxies that have a very low L_X/L_B ratio as “X-ray faint.” In these X-ray faint ellipticals, much of the hot interstellar gas may have been lost in galactic winds (Loewenstein & Mathews 1987; David, Forman, & Jones 1991) or by ram pressure stripping by ambient intracluster or intragroup gas (White & Sarazin 1991). The source of the bulk of the X-ray emission in X-ray faint galaxies is uncer-

¹ Department of Astronomy, University of Virginia, P.O. Box 3818, Charlottesville, VA 22903-0818; sarazin@virginia.edu.

² Department of Astronomy, University of Michigan, Ann Arbor, MI 48109-1090; jirwin@astro.lsa.umich.edu, jbregman@umich.edu.

³ Chandra Fellow.

tain; it might be due to low-mass X-ray binaries (LMXBs) like those seen in the bulge of our Galaxy (e.g., White, Nagase, & Parmar 1995), or to an active galactic nucleus (AGN) (Allen, di Matteo, & Fabian 2000), or to interstellar gas (Pellegrini & Fabbiano 1994), or to fainter stellar sources such as active M stars or RS CVn binaries (e.g., Pellegrini 1994).

In general, X-ray faint galaxies exhibit significantly different X-ray spectral properties than their X-ray bright counterparts. The X-ray bright galaxies are dominated by thermal emission at $kT \sim 0.8$ keV as a result of their hot ISM. On the other hand, the X-ray faint galaxies exhibit two distinct spectral components. First, they have a hard ~ 5 – 10 keV component, most easily seen in *ASCA* spectra (Matsumoto et al. 1997), which is roughly proportional to the optical luminosity of the galaxy. Actually, both X-ray faint and X-ray bright early-type galaxies appear to have this hard X-ray component, which is roughly proportional to the optical luminosity of the galaxy. This suggests that the hard component is due to LMXBs like those seen in the bulge of our Galaxy (e.g., White et al. 1995). In some cases, an AGN may contribute to the hard component (Allen et al. 2000), or it might be due to hot gas. However, the *ASCA* observations do not resolve this component into discrete sources, nor do they provide much detailed information on its spectrum. X-ray faint galaxies also have a very soft (~ 0.2 keV) component, whose origin is uncertain (Fabbiano, Kim, & Trinchieri 1994; Pellegrini 1994; Kim et al. 1996). This difference in X-ray spectral characteristics is seen in the individual X-ray spectra of a number of X-ray bright and faint galaxies and in the X-ray “colors” or hardness ratios determined for larger samples (Irwin & Sarazin 1998b). Suggested stellar sources for the very soft emission in X-ray faint ellipticals include active M stars, RS CVn binaries, or supersoft sources, but none of these appear to work quantitatively (Pellegrini & Fabbiano 1994; Irwin & Sarazin 1998a). It is possible that the soft X-rays are due to a warm (0.2 keV) ISM (Pellegrini & Fabbiano 1994). Recently, we proposed that the very soft emission in X-ray faint ellipticals might be due to the same LMXBs responsible for the hard emission (Irwin & Sarazin 1998a, 1998b). Little is known about the very soft X-ray properties of Galactic LMXBs since most lie in directions of high Galactic hydrogen column densities, so their soft X-ray emission is heavily absorbed. However, the origin of the very soft component in X-ray faint ellipticals remains something of a mystery.

With the superb spatial resolution of the *Chandra X-Ray Observatory*, it should be possible to resolve the emission from nearby X-ray faint early-type galaxies into LMXBs, if this is indeed the source of their emission. The clear test of the origin of the X-ray emission from X-ray faint ellipticals is to see if it resolves into discrete LMXBs. If the hard and/or soft X-ray emission from X-ray faint galaxies is due to LMXBs, it should come from a relatively small number of individually bright sources. Recently, we used a deep *ROSAT* HRI observation to detect a number of discrete X-ray sources in the nearby, optically luminous, X-ray faint elliptical NGC 4697 (Irwin, Sarazin, & Bregman 2000, hereafter ISB00). However, the bulk of the X-ray emission was not resolved. In ISB00, we also simulated a 40 ks *Chandra* observation of NGC 4697 and showed that it should be possible to detect ~ 100 LMXBs if they provide the bulk of the emission. Here we present the results of exactly this observation. At a distance of 15.9 Mpc (Faber et al. 1989;

assuming a Hubble constant of $50 \text{ km s}^{-1} \text{ Mpc}^{-1}$), NGC 4697 is among the closest optically luminous, X-ray faint early-type galaxies. Given its proximity, NGC 4697 is an ideal target for detecting the LMXB population. It is sufficiently X-ray faint that diffuse ISM emission should not bury the emission of the fainter LMXBs. It should be possible to detect the LMXB population down to a luminosity of $\sim 5 \times 10^{37} \text{ ergs s}^{-1}$. The purposes of the *Chandra* observation are to resolve and study the LMXB population of NGC 4697, to determine the source of both the hard and soft spectral components, and to detect or place strong limits on any residual diffuse (possibly gaseous) emission.

Some initial results of these observations were presented in Sarazin, Irwin, & Bregman (2000, hereafter Paper I). In the present paper we give the detailed properties of the sources. In § 2 the observations and data analysis are described. The overall X-ray image is discussed in § 3. The properties of the resolved sources are given in § 4, while the remaining unresolved emission is analyzed in § 5. In § 6 the X-ray spectral properties of the galaxy are derived. The interpretation of the results is discussed in § 7, and our conclusions are summarized in § 8.

2. OBSERVATION AND DATA REDUCTION

NGC 4697 was observed on 2000 January 15–16 with the ACIS-23678 chips operated at a temperature of -110°C and with a frame time of 3.2 s. The pointing was determined so that the entire galaxy was located on the S3 chip and so that the center of the galaxy was not on a node boundary of the chip. Although a number of serendipitous sources are seen on the other chips, the analysis of NGC 4697 in this paper will be based on data from the S3 chip alone. The total exposure for the S3 chip was 39,434 s. The data were telemetered in Faint mode, and only events with *ASCA* grades of 0, 2, 3, 4, and 6 were included. We excluded bad pixels, bad columns, and the columns next to bad columns and to the chip node boundaries. We checked for periods of incorrect aspect solution, and none were found. The ACIS S3 chip is known to experience occasional periods of high background (Markevitch 2000;⁴ Markevitch et al. 2000). We searched for such background flares by determining the light curve of the total count rate in the S3 chip binned in 40 s intervals; the total count rate is mainly due to background. No background flares were found, and the background rate was constant at about 0.9 s^{-1} , which was the quiescent rate for the S3 chip at the time of the observation. Only events with photon energies in the range 0.3–10 keV were included in our analysis.

This observation was processed at a time when the standard pipeline processing introduced a boresight error of about $8''$ in the absolute positions of X-ray sources. We corrected for this using optical identifications and positions of X-ray sources. As noted below (§ 4), a number of the X-ray sources have faint optical identifications. Of these, three had accurate positions given in the USNO-A2.0 optical catalog (Monet et al. 1998). The optical and X-ray positions were offset by essentially the same amount and in the same direction (to within $0.3''$). We applied the average of these offsets to the X-ray positions. We believe that the

⁴ See http://asc.harvard.edu/cal/Links/Acis/acis/Cal_prods/bkgrnd/current/index.html and <http://hea-www.harvard.edu/~maxim/axaf/acisbg>.

quoted absolute positions are accurate to about $0.5''$ near the center of the S3 image, with larger errors farther out.

Determining the background for these observations proved to be difficult. We initially tried to use background from a series of nearly “blank-sky” observations compiled by Markevitch (2000). For the S3 chip, most of the exposure in these background files occurs at high Galactic latitude, mainly from the deep survey field of Mushotzky et al. (2000). These observations were taken when the focal plane temperature was -110°C (as for our observations) and were screened to remove background flares; thus, they should be appropriate for our data. The blank-sky background file gave a surface brightness in the hard (2–10 keV) band that agreed well with the hard surface brightness in our data in outer parts of the S3 chip away from NGC 4697. However, our data had significantly more soft emission in the outer parts. In the outermost parts of the S3 chip, this extra soft emission had a fairly uniform surface brightness. While part of this emission is due to an extended soft component of NGC 4697 (§ 5.3), the constant soft surface brightness component appeared to be an additional background component. We also determined the background for the region of the I3 chip that is farthest from NGC 4697 and along its minor axis. Our data also show a soft X-ray excess in this region relative to blank-sky fields. We also examined the long *ROSAT* PSPC pointed observation of the galaxy (ISB00), which showed excess soft emission in the outer parts of the field far from NGC 4697 or other sources.

On the sky, NGC 4697 is located near the edge of the North Polar Spur (NPS), a soft X-ray Galactic feature (e.g., Snowden et al. 1997). The *ROSAT* All-Sky Survey (RASS) images of this region (e.g., Snowden et al. 1997) show a strong soft X-ray excess at the position of NGC 4697, which is consistent with the soft excess seen in the outer parts of the pointed PSPC observation. The excess is most prominent in the R4R5 *ROSAT* band, which corresponds roughly to 0.4–1 keV. The excess in the *Chandra* data is mainly in our soft band (0.3–1 keV). The level of the soft excess due to the NPS is such that it would significantly affect the background in our observation.

We used the surface brightness profile of NGC 4697 in various energy bands in both the *ROSAT* PSPC observation and in our *Chandra* data to determine the portion of the extended soft emission that was due to the NPS and the portion that was due to NGC 4697. Simple thermal models with temperatures of $\sim 2 \times 10^6$ K and a variety of abundances were used to convert the count rates for the soft excess between *ROSAT* and *Chandra*. In the outer parts of the S3 chip, we found that 55% of the soft excess was due to the NPS, while 45% was due to NGC 4697. For studying the properties of extended diffuse emission, we determine the background by combining the blank-sky background of Markevitch (2000) with background determined from the outer portion of the S3 chip in our observation and weighted by 45% and 55%, respectively. We added a systematic error to the background statistical error based on the difference in these two determinations of the background.

In determining the properties of the resolved sources (§ 4), background for each source was determined from a region around the source. This background properly includes all sources of diffuse emission, including the diffuse emission from NGC 4697. This also avoids the problem of the effect of the NPS as discussed above.

All of the X-ray spectra were extracted using the PI values for the events in order to correct for gain variations over the S3 chip. The PI values were recomputed using the gain file *acisD1999-09-16gainN0004.fits*, appropriate for an operating temperature of -110°C and a frame time of 3.2 s. The spectral responses were based on the FITS Embedded Function (FEF) files *FP-110_D1999-09-16fef_piN0002*. All of the spectra discussed here are extracted from extended regions, which cover many of the 32×32 pixel regions covered by individual FEFs. We used the RUNEXTR-SPEC software package kindly provided by Alexey Vikhlinin (Vikhlinin, Markevitch, & Murray 2001), to extract spectra and to determine the response matrices. This program weights the response files by the number of counts in each region.

3. X-RAY IMAGE

The raw *Chandra* S3 chip X-ray image was shown in Figure 1 of Paper I. This image showed the basic result of the *Chandra* observation: much of the emission from the galaxy is resolved into individual point sources of X-rays. The raw X-ray image of a $1' \times 1'$ central region of the NGC 4697 is shown in Figure 1. The gray scale is proportional to the square root of the X-ray surface brightness, and the values vary between 1 and 25 counts pixel^{-1} . The numbers identify the detected sources in this regions as listed in Table 1. The optical center of the galaxy coincides with the position of source 1. The center of the image has been offset from the optical because there are more sources to the east-northeast than west-southwest of the galaxy center. The density of resolved sources near the center of the galaxy is high, and they may become confused in this region.

In order to image the fainter, more diffuse emission, we adaptively smoothed the entire *Chandra* S3 X-ray image to a minimum signal-to-noise ratio (S/N) of 3 per smoothing beam. The image was corrected for exposure and background. Regions with an exposure of less than 20 ks were removed to avoid artifacts at the chip edges. This adaptively smoothed image is shown in Figure 2. The gray scale is logarithmic and covers surface brightnesses that range over a factor of $\gtrsim 4000$. The central $4' \times 4'$ region of the adaptively smoothed image was presented as Figure 2 in Paper I, showing only the brighter regions.

For comparison, Figure 3 shows the Digital Sky Survey (DSS) optical image of the same region as shown in Figure 2. The circles indicate the positions of individual X-ray sources, which are identified in § 4 and Table 1. The distribution of X-ray point sources in Figure 1 of Paper I appears to be elongated at the same position angle (P.A.) as the optical image of this E6 galaxy (67° ; Jedrzejewski, Davies, & Illingworth 1987; Faber et al. 1989; Peletier et al. 1990); this is discussed in detail in § 4.6. (The small background galaxy LCRS B124537.4–053024, which is located at the right side of Figure 3, is beyond the edge of the S3 chip.)

Figures 1 and 2, as well as Figure 1 of Paper I, show that the X-ray emission from NGC 4697 is mainly due to resolved sources, which are discussed in more detail in § 4. However, there is also some spatially extended, unresolved emission. Near the center of the image (Fig. 2, Paper I), the unresolved emission follows the elliptical distribution of optical light in the galaxy. However, at larger radii the unresolved emission becomes somewhat irregular and has something of an “L-shaped” distribution, with extension to the

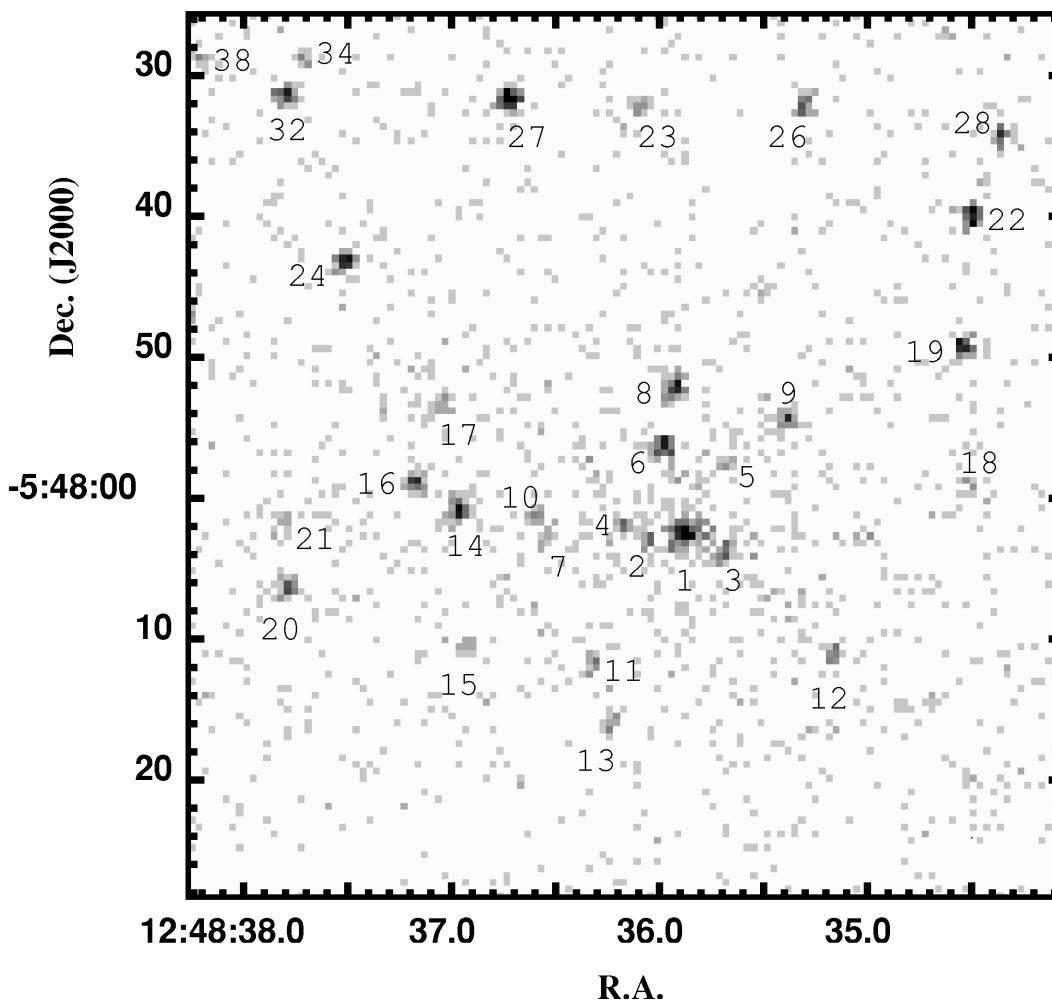


FIG. 1.—*Chandra* S3 image of an approximately $1' \times 1'$ region near the center of NGC 4697. The gray scale varies with the square root of the X-ray surface brightness, which ranges from 1 to 25 counts pixel⁻¹. (The ACIS pixels are $0''.492$ square.) The positions of detected sources in the image are indicated by their source numbers in Table 1; the source numbers are ordered by increasing distance from the center of the galaxy. Source 1 is located at the optical center of the galaxy.

east and south. The unresolved emission also is more extended than the optical light of the galaxy at the same relative surface brightness levels, particularly along the optical minor axis of the galaxy. The spatial distribution of the unresolved emission is discussed in more detail in § 5.3.

4. RESOLVED SOURCES

4.1. Detections

The discrete X-ray source population on the ACIS S3 image (Fig. 1, Paper I) was determined, using both cell detection and wavelet detection algorithms. We used the CIAO CELLDETECT and WAVDETECT programs. The two techniques gave consistent source lists with nearly identical fluxes. For sources located in the dense central region of NGC 4697 where confusion and the effect of an enhanced background due to unresolved sources or diffuse emission were important, the wavelet technique worked slightly better. The wavelet source detection threshold was set at 10^{-6} , which implies that less than or approximately one false source (due to a statistical fluctuation in the background) would be detected in the entire S3 image. This corresponded to requiring that the sources be detected at the $\geq 3\sigma$ level. The CELLDETECT threshold was initially

taken to be $\geq 2\sigma$, but the resulting source list was culled to remove sources whose signal-to-noise ratio was less than 3σ . While variations in the background, exposure, and instrumental point-spread function (PSF) across the image cause the minimum detectable flux to vary somewhat with position, over most of the galaxy the minimum detectable flux was about 2.6×10^{-4} counts s⁻¹ ($L_X = 5.0 \times 10^{37}$ ergs s⁻¹ at the NGC 4697 distance) in the 0.3–10 keV band. Fluxes were corrected for exposure and the instrument PSF. The detection limit is higher at the edges of the field and at the southern and western ends of the image, where the instrumental PSF is larger than near the aim point. All of the source detections were verified by examining the image.

Table 1 lists the 90 discrete sources detected by this technique, sorted in order of increasing distance d from the center of NGC 4697. Columns (1)–(9) give the source number, the IAU name, the source position (R.A. and decl., J2000), the projected distance d from the center of NGC 4697, the projected isophotal semimajor axis a (see § 4.6), the count rate and the 1σ error, the S/N for the count rate, and the unabsorbed 0.3–10 keV X-ray luminosity L_X (assuming the source is located at the distance of NGC 4697; see § 4.3). The conversion to luminosities assumes the best-fit source spectrum (thermal bremsstrahlung with

TABLE 1
DISCRETE X-RAY SOURCES

Source (1)	Name (2)	R.A. (3)	Decl. (4)	d (arcsec) (5)	a (arcsec) (6)	Count Rate (10^{-4} s^{-1}) (7)	S/N (8)	L_x (0.3–10 keV) ($10^{37} \text{ ergs s}^{-1}$) (9)	ISB00 Source (10)	Notes (11)
1	CXOU J124835.8–054802	12 48 35.87	–5 48 02.4	0.00	0.00	41.88±3.35	12.51	80.35	7	1, 2, 3
2	CXOU J124836.0–054803	12 48 36.06	–5 48 03.0	2.80	3.64	5.03±1.17	4.32	9.66	...	2, 4
3	CXOU J124835.6–054803	12 48 35.68	–5 48 03.7	3.13	3.12	13.88±1.96	7.09	26.63	...	2, 3
4	CXOU J124836.1–054801	12 48 36.17	–5 48 01.9	4.51	4.87	5.03±1.19	4.21	9.65	...	2
5	CXOU J124835.7–054757	12 48 35.72	–5 47 57.6	5.32	9.16	3.60±1.11	3.25	6.91	...	2
6	CXOU J124835.9–054756	12 48 35.98	–5 47 56.3	6.26	9.32	18.39±2.23	8.23	35.28	8?	2
7	CXOU J124836.5–054802	12 48 36.54	–5 48 02.6	9.90	11.46	3.19±0.99	3.23	6.11	...	2
8	CXOU J124835.9–054752	12 48 35.93	–5 47 52.1	10.36	16.53	16.78±2.13	7.88	32.18	8?	2
9	CXOU J124835.4–054754	12 48 35.40	–5 47 54.5	10.65	17.69	9.20±1.63	5.65	17.66	...	2, 3, 4
10	CXOU J124836.6–054801	12 48 36.60	–5 48 01.9	10.89	11.81	4.41±1.11	3.97	8.45	...	2
11	CXOU J124836.3–054811	12 48 36.32	–5 48 11.7	11.51	19.54	3.99±1.08	3.69	7.66	...	2
12	CXOU J124835.1–054811	12 48 35.16	–5 48 11.1	13.71	14.72	5.77±1.29	4.46	11.07	...	2
13	CXOU J124836.2–054815	12 48 36.23	–5 48 15.9	14.50	25.02	3.80±1.05	3.61	7.29	...	2
14	CXOU J124836.9–054800	12 48 36.97	–5 48 00.8	16.36	17.77	16.93±2.16	7.85	32.47	...	2, 3
15	CXOU J124836.9–054810	12 48 36.93	–5 48 10.5	17.69	26.02	3.33±1.02	3.37	6.38	...	2
16	CXOU J124837.1–054758	12 48 37.17	–5 47 58.8	19.68	20.61	11.32±1.76	6.43	21.71	...	5
17	CXOU J124837.0–054753	12 48 37.05	–5 47 53.4	19.74	19.84	4.61±1.16	3.96	8.85	...	2
18	CXOU J124834.5–054759	12 48 34.51	–5 47 59.0	20.62	25.80	3.16±1.02	3.10	6.07	...	2, 4
19	CXOU J124834.5–054749	12 48 34.54	–5 47 49.3	23.87	36.72	15.62±2.06	7.60	29.97	...	4, 5
20	CXOU J124837.7–054806	12 48 37.79	–5 48 06.3	28.91	35.65	9.33±1.61	5.81	17.90	...	
21	CXOU J124837.8–054801	12 48 37.83	–5 48 01.6	29.25	32.93	3.28±1.02	3.22	6.28	...	
22	CXOU J124834.5–054739	12 48 34.50	–5 47 39.9	30.42	50.44	19.32±2.27	8.53	37.07	...	
23	CXOU J124836.0–054732	12 48 36.09	–5 47 32.1	30.47	48.20	4.89±0.71	4.10	9.37	...	
24	CXOU J124837.5–054743	12 48 37.51	–5 47 43.2	31.07	33.09	15.92±2.06	7.72	30.55	...	
25	CXOU J124836.1–054833	12 48 36.11	–5 48 33.5	31.35	52.58	6.65±1.49	4.47	12.76	...	
26	CXOU J124835.3–054732	12 48 35.30	–5 47 32.0	31.55	54.08	8.36±1.51	5.55	16.04	...	4
27	CXOU J124836.7–054731	12 48 36.72	–5 47 31.6	33.22	46.68	31.25±2.86	10.91	59.95	...	4
28	CXOU J124834.3–054734	12 48 34.35	–5 47 34.2	36.15	60.75	8.55±1.53	5.59	16.41	...	
29	CXOU J124833.3–054802	12 48 33.35	–5 48 02.2	37.65	43.09	5.80±1.36	4.26	11.13	...	
30	CXOU J124838.3–054747	12 48 38.30	–5 47 47.2	39.29	39.29	5.80±1.29	4.48	11.13	...	
31	CXOU J124833.3–054816	12 48 33.32	–5 48 16.1	40.55	40.68	6.38±1.46	4.37	12.23	...	
32	CXOU J124837.8–054731	12 48 37.80	–5 47 31.3	42.32	48.83	13.02±1.87	6.98	24.97	...	
33	CXOU J124833.9–054833	12 48 33.93	–5 48 33.8	42.80	49.38	3.02±0.93	3.25	5.79	...	
34	CXOU J124837.7–054728	12 48 37.71	–5 47 28.8	43.33	51.86	2.89±0.92	3.16	5.55	...	
35	CXOU J124838.6–054746	12 48 38.68	–5 47 46.6	44.70	44.80	8.02±1.48	5.42	15.38	...	
36	CXOU J124833.2–054741	12 48 33.21	–5 47 41.7	44.82	66.03	51.05±3.65	14.00	97.92	5	4
37	CXOU J124836.4–054847	12 48 36.48	–5 48 47.1	45.63	77.63	8.29±1.60	5.18	15.90	...	6
38	CXOU J124838.2–054728	12 48 38.22	–5 47 28.8	48.51	54.25	3.66±1.05	3.50	7.02	...	
39	CXOU J124839.0–054749	12 48 39.03	–5 47 49.9	48.77	49.79	5.69±1.27	4.49	10.92	...	
40	CXOU J124839.3–054806	12 48 39.32	–5 48 06.9	51.68	61.94	48.02±3.53	13.61	92.11	9	6
41	CXOU J124834.9–054859	12 48 34.92	–5 48 59.2	58.57	88.01	12.17±1.82	6.67	23.35	...	
42	CXOU J124839.3–054730	12 48 39.35	–5 47 30.2	61.00	62.44	16.75±2.11	7.95	32.13	...	
43	CXOU J124839.9–054738	12 48 39.92	–5 47 38.0	65.18	65.19	7.94±1.46	5.45	15.24	...	
44	CXOU J124839.0–054714	12 48 39.03	–5 47 14.1	67.41	76.70	9.53±1.60	5.94	18.27	...	
45	CXOU J124832.6–054851	12 48 32.66	–5 48 51.0	68.32	77.43	11.32±1.75	6.46	21.72	4	
46	CXOU J124831.8–054838	12 48 31.85	–5 48 38.6	70.08	71.43	2.76±0.90	3.08	5.30	...	
47	CXOU J124831.7–054846	12 48 31.74	–5 48 46.8	76.02	79.56	10.51±1.70	6.19	20.15	...	
48	CXOU J124837.8–054652	12 48 37.88	–5 46 52.2	76.35	106.53	3.45±0.98	3.51	6.62	...	
49	CXOU J124831.0–054828	12 48 31.04	–5 48 28.8	76.82	76.99	4.18±1.10	3.81	8.01	...	6
50	CXOU J124840.8–054822	12 48 40.88	–5 48 22.7	77.41	102.56	2.76±0.88	3.13	5.30	...	
51	CXOU J124840.9–054731	12 48 40.93	–5 47 31.0	81.74	81.77	5.22±1.19	4.39	10.01	...	4, 6
52	CXOU J124841.2–054819	12 48 41.27	–5 48 19.4	82.28	105.63	11.24±1.73	6.50	21.56	...	4, 5
53	CXOU J124830.8–054836	12 48 30.82	–5 48 36.9	82.91	82.96	25.75±2.62	9.84	49.40	2	6, 7
54	CXOU J124834.2–054926	12 48 34.23	–5 49 26.2	87.34	128.94	3.61±1.10	3.28	6.92	...	6, 7
55	CXOU J124841.5–054736	12 48 41.50	–5 47 36.8	87.82	88.77	2.70±0.88	3.07	5.17	...	4, 6, 7
56	CXOU J124839.2–054645	12 48 39.22	–5 46 45.2	91.93	117.05	3.93±1.07	3.66	7.54	...	
57	CXOU J124833.2–054627	12 48 33.23	–5 46 27.8	102.45	176.64	10.16±1.64	6.21	19.49	...	
58	CXOU J124843.2–054808	12 48 43.22	–5 48 08.8	109.76	129.36	4.21±1.08	3.89	8.08	...	4
59	CXOU J124833.0–054614	12 48 33.00	–5 46 14.3	116.30	200.48	3.87±1.02	3.78	7.42	...	
60	CXOU J124829.1–054704	12 48 29.10	–5 47 04.6	116.47	174.71	2.62±0.86	3.06	5.02	...	
61	CXOU J124835.9–054551	12 48 35.93	–5 45 51.5	130.93	213.59	13.68±1.89	7.24	26.23	...	4, 6, 7
62	CXOU J124832.4–055004	12 48 32.42	–5 50 04.2	132.27	184.92	8.56±1.64	5.22	16.42	...	
63	CXOU J124828.7–054922	12 48 28.72	–5 49 22.1	133.23	140.44	7.46±1.51	4.94	14.31	...	
64	CXOU J124834.4–055014	12 48 34.42	–5 50 14.1	133.48	207.13	17.34±2.24	7.73	33.25	...	4, 6, 7

TABLE 1—Continued

Source (1)	Name (2)	R.A. (3)	Decl. (4)	d (arcsec) (5)	a (arcsec) (6)	Count Rate (10^{-4} s^{-1}) (7)	S/N (8)	L_x (0.3–10 keV) ($10^{37} \text{ ergs s}^{-1}$) (9)	ISB00 Source (10)	Notes (11)
65.....	CXOU J124827.3–054707	12 48 27.34	–5 47 07.7	138.58	197.35	26.98 ± 2.68	10.08	51.76	1	
66.....	CXOU J124841.4–054602	12 48 41.43	–5 46 02.9	145.44	181.78	7.86 ± 1.44	5.47	15.07	...	
67.....	CXOU J124826.1–054729	12 48 26.15	–5 47 29.4	148.80	192.57	3.67 ± 1.10	3.34	7.05	...	6, 7
68.....	CXOU J124825.5–054808	12 48 25.51	–5 48 08.8	154.85	172.71	3.27 ± 1.02	3.22	6.28	...	
69.....	CXOU J124827.0–054925	12 48 27.04	–5 49 25.7	155.87	159.82	23.51 ± 2.59	9.08	45.11	...	6, 7
70.....	CXOU J124846.5–054811	12 48 46.54	–5 48 11.5	159.40	187.77	3.58 ± 0.99	3.59	6.86	...	
71.....	CXOU J124834.3–055051	12 48 34.32	–5 50 51.8	170.98	267.92	18.07 ± 2.34	7.72	34.67	6	6
72.....	CXOU J124846.8–054852	12 48 46.86	–5 48 52.9	171.50	231.36	82.08 ± 4.65	17.66	157.46	11	4, 6, 8
73.....	CXOU J124824.1–054816	12 48 24.18	–5 48 16.8	175.09	191.32	6.04 ± 1.37	4.40	11.60	...	
74.....	CXOU J124828.7–055025	12 48 28.75	–5 50 25.8	178.53	219.11	7.24 ± 1.50	4.81	13.88	...	
75.....	CXOU J124826.0–055001	12 48 26.02	–5 50 01.2	189.03	202.62	4.94 ± 1.23	4.02	9.48	...	6
76.....	CXOU J124823.7–054659	12 48 23.74	–5 46 59.6	191.63	263.26	14.70 ± 2.03	7.25	28.20	...	
77.....	CXOU J124845.4–054541	12 48 45.44	–5 45 41.9	200.30	225.34	28.64 ± 2.72	10.53	54.94	10	4
78.....	CXOU J124822.4–054815	12 48 22.48	–5 48 15.7	200.30	220.53	23.52 ± 2.60	9.06	45.12	...	4
79.....	CXOU J124822.4–054838	12 48 22.49	–5 48 38.2	202.89	212.50	4.51 ± 1.25	3.60	8.65	...	
80.....	CXOU J124825.4–054551	12 48 25.42	–5 45 51.6	203.59	326.05	3.22 ± 0.95	3.41	6.19	...	
81.....	CXOU J124822.8–054652	12 48 22.83	–5 46 52.8	206.77	285.40	6.27 ± 1.38	4.56	12.04	...	
82.....	CXOU J124824.4–054557	12 48 24.44	–5 45 57.9	211.22	330.79	133.53 ± 5.98	22.34	256.15	...	4
83.....	CXOU J124837.5–054430	12 48 37.54	–5 44 30.9	212.96	335.92	3.16 ± 0.93	3.41	6.06	...	
84.....	CXOU J124847.2–055014	12 48 47.23	–5 50 14.0	214.60	339.59	7.29 ± 1.46	4.91	13.98	...	4
85.....	CXOU J124847.4–054512	12 48 47.47	–5 45 12.4	242.55	272.78	16.19 ± 3.22	5.02	31.05	12	9
86.....	CXOU J124819.6–054733	12 48 19.60	–5 47 33.3	244.61	298.39	3.80 ± 1.11	3.43	7.30	...	
87.....	CXOU J124842.9–055158	12 48 42.97	–5 51 58.4	258.63	445.89	4.36 ± 1.42	3.06	8.36	...	
88.....	CXOU J124851.1–054548	12 48 51.12	–5 45 48.6	263.99	268.36	5.15 ± 1.22	4.22	9.88	...	6
89.....	CXOU J124817.6–054727	12 48 17.66	–5 47 27.0	274.17	336.35	10.22 ± 1.80	4.68	19.61	...	
90.....	CXOU J124828.4–054326	12 48 28.43	–5 43 26.4	297.46	512.79	8.26 ± 1.55	5.33	15.84	...	

NOTE.—Units of right ascension are hours, minutes, and seconds, and units of declination are degrees, arcminutes, and arcseconds. (1) The position of source 1 agrees with the optical center of NGC 4697 to within the errors. (2) Positions and fluxes of sources near the center of NGC 4697 are uncertain as a result of crowding. (3) This source appears to be extended, although this may be due to confusion with other sources or the effect of diffuse emission. (4) Source may be variable. (5) Supersoft source. (6) Possible faint optical counterpart. (7) Globular cluster is possible optical counterpart. (8) The optical ID of this source is an AGN at redshift $z = 0.696$. (9) This source is at the edge of the S3 detector, and its flux is uncertain as a result of a large exposure correction. Table 1 is also available in machine-readable form in the electronic edition of the *Astrophysical Journal*.

$kT = 8.1$ keV and Galactic absorption with $N_{\text{H}} = 2.12 \times 10^{20} \text{ cm}^{-2}$; § 6 and Table 4, row 3). The statistical errors in the positions of most of the sources are quite small ($\sim 0''.2$), and the overall absolute errors are probably $\sim 0.5''$ near the center of the field, with larger errors near the outside of the field. The values of the distance from the galaxy center d are actually computed from the position of source 1; its position agrees with the position of the optical center of the NGC 4697 to within the errors, but relative X-ray positions are more accurate. Thus, d might differ from the distance from the optical center of the galaxy by $\sim 1''$.

As noted above, our detection limit for sources should result in less than or approximately one false source (due to a statistical fluctuation) in the entire S3 field of view. However, many of the detected sources may be unrelated foreground or (more likely) background objects. Based on the source counts in Brandt et al. (2000) and Mushotzky et al. (2000), we would expect about 10–15 serendipitous sources in our observation. These should be spread out fairly uniformly over the S3 image (Fig. 1, Paper I), except for the effects of the reduced exposure and increased PSF at the outside of the field. Thus, the unrelated sources should mainly be found at larger distances from the optical center of NGC 4697 (the bottom part of Table 1), while the sources associated with NGC 4697 should be concentrated to the center of the galaxy. Within $2'$ of the center of NGC 4697 (roughly the region covered by Fig. 2 in Paper I), approximately two of the ~ 60 detected sources would be expected to be unrelated to NGC 4697.

4.2. Identifications

The position of source 1 agrees with the optical position of the center of NGC 4697 (R.A. = $12^{\text{h}}48^{\text{m}}35^{\text{s}}.71$, decl. = $-5^{\circ}48'02''.9$; Wegner et al. 1996) to within the combined X-ray and optical errors. Its luminosity is $L_x = 8 \times 10^{38} \text{ ergs s}^{-1}$. This source appears to be broader than the instrumental PSF (Fig. 1). On the other hand, the density of sources is quite high near the center of NGC 4697, and the apparent extension may be due to confusion with other sources or diffuse emission. It is possible that the central source is due in part to an AGN and/or to one or more LMXBs, as discussed below in § 7.1.

Near the center of the galaxy, the density of sources is quite high, and it is likely that some of the positions, fluxes, and sizes are affected by source confusion. Source 3 is very close to source 1 and also appears somewhat extended. It may be a composite or may be affected by the central source 1. Source 2 is very close to both source 1 and source 4. Sources 7 and 10 are quite close together.

ISB00 detected 12 X-ray sources around NGC 4697 using the *ROSAT* HRI, all of which lie within the field of view of the S3 image. All but one of these sources lie within a few arcseconds of strong sources that we detect with *Chandra*. The identifications of these sources (the source numbers in Table 1 from ISB00) are listed in column (10) of Table 1. ISB00 source 7 corresponds to the central X-ray source (source 1 in the present paper). ISB00 source 8 was an extended source located about $7''$ north of the center of the

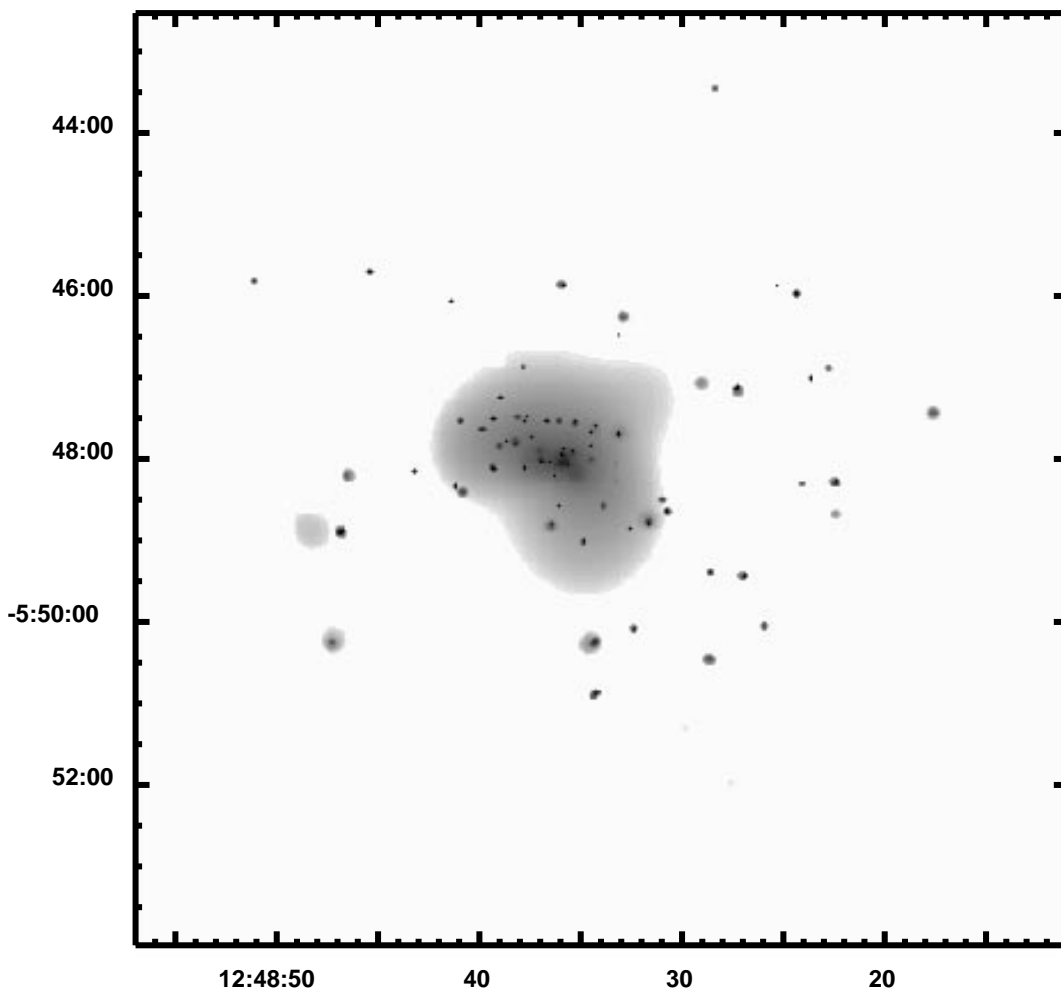


FIG. 2.—Adaptively smoothed version of the entire *Chandra* S3 X-ray image of the region around NGC 4697 in the 0.3–10 keV band. The image was adaptively smoothed to an S/N of 3 per smoothing beam and corrected for exposure and background. Regions with an exposure of less than 20 ks were removed to avoid artifacts at the chip edges. The gray scale is logarithmic and ranges from 2×10^{-7} to 10^{-3} counts pixel $^{-1}$ s $^{-1}$. (The ACIS pixels are $0''.492$ square.)

galaxy; we believe that this source is actually due to the superposition of our sources 6 and 8, with possible contributions from sources 5 and/or 9 as well. In general, the ISB00 sources have *Chandra* S3 count rates $\gtrsim 2 \times 10^{-3}$ counts s $^{-1}$ and are thus almost an order of magnitude brighter than the faintest sources we detect. ISB00 source 3 was located about $54''$ west of the center of NGC 4697. We do not detect a source or any enhancement in the background surface brightness at this location. Given that ISB00 source 3 was the least significant source detected by ISB00 (only slightly better than 2σ), it seems likely that this source was a statistical fluctuation in the *ROSAT* HRI image. Alternatively, this source may be variable and might have declined by more than an order of magnitude since the *ROSAT* observation (§ 4.5).

The positions of the X-ray sources were examined on the DSS image of this region (Fig. 3). A total of 11 of the sources had possible faint optical counterparts on this image; four others appear on deeper optical images discussed below. These are all marked with footnote e in Table 1. The possible faint optical counterparts of sources 71 and 72 were noted previously by ISB00. None of the sources corresponded to objects listed on NED or SIMBAD.

However, several of the X-ray sources coincide with candidate globular clusters associated with NGC 4697. Source 64 has a faint optical counterpart on the DSS image that agrees with the position of globular cluster candidate 33 from the catalog of Hanes (1977). (However, this source has an unusual X-ray spectrum, which may indicate that it is actually a background AGN; see § 4.4.) Most of the Hanes (1977) globulars are fairly bright and located at relatively large distances from NGC 4697. J. Kavelaars (2000, private communication) gives a list of generally fainter candidate globular clusters located between $1'.5$ and $2'.5$ from the center of NGC 4697. By comparing this list with the X-ray source positions, we find faint candidate globular clusters located within $1''$ of the positions of X-ray sources 53, 54, 55, 61, 64, 67, and 69. The globular cluster associated with source 64 is the same one listed by Hanes (1977). Given the density of candidate globulars and the very good position agreement, one would expect ~ 0.3 associations to occur at random. Thus, it is likely that all of the seven associations of X-ray sources with optical globular cluster candidates in Table 1 are real. However, at the distance to NGC 4697, globular clusters are not resolved in ground-based optical images, and the candidate globulars were identified by lumi-

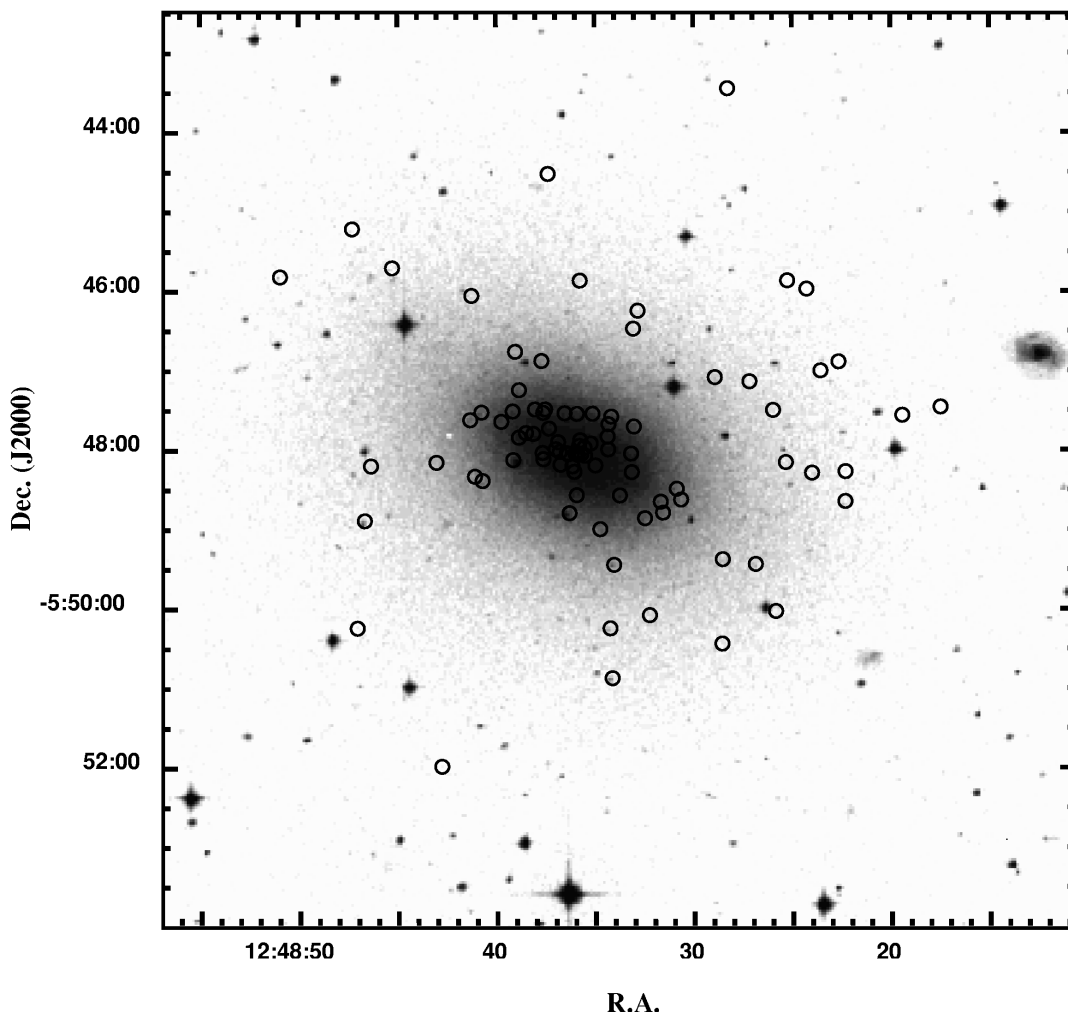


FIG. 3.—DSS optical image of NGC 4697, showing the same field as in Fig. 2 or Fig. 1 in Paper I. The circles show the positions of the discrete X-ray sources listed in Table 1.

nosities and (possibly) colors. As a result, as many as half of them might be unrelated faint optical objects, rather than globular clusters.

An example of such a misidentified globular cluster is the optical object associated with source 72. Hanes (1977) lists this object as a candidate globular cluster (24), although it would be rather bright for a globular at the distance of NGC 4697. Moreover, the USNO-A2.0 optical catalog (Monet et al. 1998) indicates that this source has a very blue color ($B-R \approx -0.7$), which is bluer than even a Rayleigh-Jeans spectrum and would be unheard of for a globular cluster. An optical spectrum kindly provided by C. Mullis (2000, private communication) shows that this object is a background AGN at a redshift of $z = 0.696$, rather than a globular cluster. The very blue color is due in part to a strong Mg II $\lambda 2798$ line in the spectrum, redshifted into the B band.

4.3. Luminosities and Luminosity Function

The count rates for the sources were converted into unabsorbed luminosities (0.3–10 keV) assuming that all of the sources were at the distance of NGC 4697, which we take to be 15.9 Mpc (Faber et al. 1989; $H_0 = 50 \text{ km s}^{-1} \text{ Mpc}^{-1}$). We adopted the best-fit *Chandra* X-ray spectrum of the

resolved sources within the inner one effective radius (Table 4, row 3). The resulting factor for converting the count rate (0.3–10 keV) into the unabsorbed luminosity L_X (0.3–10 keV) was $1.92 \times 10^{41} \text{ ergs count}^{-1}$. The resulting X-ray luminosities are given in column (9) of Table 1 and range from about 5×10^{37} to $2.5 \times 10^{39} \text{ ergs s}^{-1}$. The cumulative luminosity function of all of the sources was shown as a histogram in Figure 3 of Paper I. There we found that the luminosity function of the NGC 4697 sources could not be fitted by a single power law, as the luminosity function has a “knee” at $L_X \approx 3 \times 10^{38} \text{ ergs s}^{-1}$. A broken power law,

$$\frac{dN}{dL_{38}} = N_o \begin{cases} \left(\frac{L_{38}}{L_b}\right)^{-\alpha_l}, & L_{38} \leq L_b, \\ \left(\frac{L_{38}}{L_b}\right)^{-\alpha_h}, & L_{38} > L_b, \end{cases} \quad (1)$$

gave a good fit, where L_{38} is the X-ray luminosity (0.3–10 keV) in units of $10^{38} \text{ ergs s}^{-1}$. The best fit, determined by the maximum likelihood method, gave $N_o = 8.0_{-5.2}^{+7.1}$, $\alpha_l = 1.29_{-0.49}^{+0.36}$, $\alpha_h = 2.76_{-0.39}^{+1.81}$, and a break luminosity of $L_b = 3.2_{-0.8}^{+2.0} \times 10^{38} \text{ ergs s}^{-1}$. We also determined the luminosity functions for sources within the optical half-light elliptical isophote and for sources at larger distances. The errors were

increased significantly (particularly for the outer region), but the luminosity functions agreed with the one shown in Figure 3 of Paper I.

4.4. Hardness Ratios of Sources

We studied the crude spectral properties of the resolved sources by using hardness ratios. Hardness ratios or X-ray colors have the advantage that they can be applied to weaker sources. We defined two hardness ratios as $H21 \equiv (M - S)/(M + S)$ and $H31 \equiv (H - S)/(H + S)$, where S , M , and H are the total counts in our soft (0.3–1 keV), medium (1–2 keV), and hard (2–10 keV) bands, respectively. The hardness ratios of the sources and 90% confidence regions are listed in Table 2 (see also Fig. 4 in Paper I). For comparison, the hardness ratios (H21, H31) are (–0.38, –0.57) for all of the emission, (–0.69, –0.82) for the unresolved emission, and (–0.14, –0.37) for the sum of the sources, all within one effective radius (§ 5).

There are three moderate-luminosity sources with hardness ratios of (–1, –1), which means that they have no detectable emission beyond 1 keV. For example, a black-body spectrum with a temperature of 0.1 keV and the Galactic absorption toward NGC 4697 ($N_{\text{H}} = 2.12 \times 10^{20} \text{ cm}^{-2}$) would give hardness ratios of (H21, H31) \approx (–0.97, –1.00). These three sources, sources 16, 19, and 52, are almost certainly supersoft sources (e.g., Kahabka & van den Heuvel 1997). All three are located at small enough distances from the center of NGC 4697 that they are likely to be associated with the galaxy. Sources 19 and 52 also may be variable (§ 4.5). We believe that this observation represents the first detection of supersoft sources in a luminous elliptical galaxy.

There are three sources with hardness ratios of $\sim(1, 1)$, one of which is the brightest source in the field (source 82). These are sources 82, 83, and 90. As is clear from their source numbers, all of these sources are located far (greater than 3.5) from the center of NGC 4697. These are probably unrelated, strongly absorbed AGNs, similar to the sources that produce the hard component of the X-ray background and appear strongly at the faint fluxes in the deep *Chandra* observations of blank fields (Brandt et al. 2000; Mushotzky et al. 2000; Giacconi et al. 2001). As a comparison, a power-law spectrum with a photon spectral index $\Gamma = 1.5$ and with an absorbing column of $N_{\text{H}} = 10^{22} \text{ cm}^{-2}$ gives hardness ratios of (H21, H31) \approx (0.88, 0.92).

There are eight sources (sources 13, 50, 64, 66, 68, 74, 85, and 89) with hardness ratios near (0, –1) that have essentially no hard emission. For example, a power-law spectrum with a photon spectral index $\Gamma = 3.5$ and with an absorbing column of $N_{\text{H}} = 3 \times 10^{21} \text{ cm}^{-2}$ gives hardness ratios of (H21, H31) \approx (–0.18, –0.81). Six of these sources are at large radii (greater than 2.2), which suggests that most of this population is also unrelated to NGC 4697. The hardness ratios for these sources are consistent with the soft-band-only sources seen in the Giacconi et al. (2001) deep field at similar flux levels. However, note that source 64 was also identified with a candidate globular cluster in NGC 4697; perhaps this source is a globular cluster LMXB with an unusual X-ray spectrum, or the optical counterpart may be a background AGN rather than a globular. (Note that the 11 possible background sources selected by colors in the last two paragraphs plus the AGN [source 72] would account for most of the ~ 10 –15 unrelated sources expected based on deep blank-sky observations.)

Most of the sources lie in a diagonal swath centered at about (–0.15, –0.40). Note that hardness ratios of (–0.14, –0.37) correspond to the cumulative source spectrum with one effective radius (Table 4, row 3). This is a hard spectrum fit by thermal bremsstrahlung with $kT = 8.1 \text{ keV}$ and Galactic absorption with $N_{\text{H}} = 2.12 \times 10^{20} \text{ cm}^{-2}$. These values are similar to but slightly harder than the integrated colors or the entire galaxy, but they are considerably harder than the values for the unresolved emission. There may be some tendency for the fainter sources to have higher H/M ratios than the brighter sources.

4.5. Variability of Sources

We searched for variability in the X-ray emission of the resolved sources over the duration of the *Chandra* observation using the K-S test. This test can detect a variation in the flux from the source over the ~ 11 hr duration of the observation, such as a secular increase in the flux or a sudden turn-on or turnoff of the source. In terms of the phenomenology of LMXBs in our Galaxy, one might detect orbital variations or other secular variations. Although we could, in principal, detect a type I X-ray burster, the luminosities (typically less than or approximately the Eddington luminosity of a neutron star [NS]) and durations (10 – 10^3 s) imply that we would expect $\lesssim 1$ count from a burst at the distance of NGC 4697. The K-S test cannot detect short-term variations in the source that do not individually contribute significantly to the total number of counts. For example, we could not detect periodic pulses due to rotational modulation of an accreting NS. In principal, other tests could be done to search for pulsations from some of the brighter sources; in practice this is difficult because of the 3.2 s periodicity on the events imposed by the CCD readout. We found that 11 sources were inconsistent with a constant flux at greater than 90% confidence; these sources are noted in Table 1. In Figure 4 we show the histogram of the total counts from the five sources with more than 20 net counts and with variability detected at greater than 95% confidence.

We also tested for variability over longer timescales by comparing the *Chandra* count rates of the sources with detections or limits from a long (78,744 s) *ROSAT* HRI observation of the galaxy on 1997 June 19–July 20 (ISB00). We considered the sources as variable if they increased or decreased by greater than 50% at greater than 1σ significance. Sources with significantly higher fluxes at the time of the *Chandra* observation were sources 19, 27, 52, 61, 64, 72 (ISB00 source 11), 78, and 82. Source 64 also appeared to vary during the *Chandra* observation. Both sources 19 and 52 are supersoft sources. The third supersoft source (source 16) also showed some evidence for variability, but not at a significant level.

4.6. Spatial Distribution of Sources

One might expect the stellar X-ray sources associated with NGC 4697 to have a spatial distribution that is very similar to that of the optical light. Unfortunately, the spatial distribution of detected X-ray sources may also be affected by variations in the sensitivity limit as a result of variations in exposure, the instrumental PSF, and the diffuse background and emission. Because of these possible problems and statistical limits due to the number of sources, we limit this discussion to a few simple comparisons of the X-ray source and optical distributions. We consider only sources

TABLE 2
HARDNESS RATIOS FOR SOURCES

Source	H21	H31	Source	H21	H31	Source	H21	H31
1	-0.22(-0.31, -0.13)	-0.34(-0.42, -0.25)	32	0.02(-0.17, 0.21)	-0.33(-0.52, -0.15)	62	0.00(-0.30, 0.30)	-0.21(-0.51, 0.10)
2	0.01(-0.32, 0.34)	-0.68(-1.00, -0.36)	33	-0.30(-0.70, 0.10)	-0.71(-1.00, -0.22)	63	-0.38(-0.65, -0.12)	-0.18(-0.46, 0.10)
3	-0.44(-0.58, -0.30)	-0.69(-0.83, -0.56)	34	0.19(-0.31, 0.69)	-0.03(-0.73, 0.67)	64	-0.05(-0.20, 0.10)	-0.92(-1.00, -0.78)
4	-0.03(-0.33, 0.27)	-0.42(-0.71, -0.14)	35	-0.18(-0.39, 0.04)	-0.53(-0.75, -0.31)	65	0.24(0.14, 0.35)	-0.30(-0.44, -0.15)
5	-0.21(-0.55, 0.12)	-0.09(-0.44, 0.26)	36	0.03(-0.06, 0.12)	-0.26(-0.35, -0.18)	66	0.07(-0.17, 0.31)	-0.83(-1.00, -0.55)
6	0.00(-0.16, 0.16)	-0.32(-0.47, -0.18)	37	-0.16(-0.37, 0.06)	-0.67(-0.90, -0.45)	67	0.10(-0.87, 1.00)	0.39(-0.23, 1.00)
7 and 10 ^a	-0.11(-0.33, 0.12)	-0.67(-0.90, -0.44)	38	-0.21(-0.55, 0.12)	-0.35(-0.70, 0.00)	68	0.30(-0.12, 0.71)	-1.00(-1.00, -0.07)
8	0.17(0.01, 0.32)	-0.01(-0.21, 0.19)	39	0.19(-0.07, 0.45)	-0.25(-0.60, 0.10)	69	0.07(-0.07, 0.21)	-0.22(-0.37, -0.06)
9	-0.62(-0.74, -0.49)	-0.87(-1.00, -0.75)	40	0.02(-0.07, 0.12)	-0.23(-0.32, -0.14)	70	-0.10(-0.56, 0.36)	-0.04(-0.53, 0.45)
11	-0.07(-0.40, 0.27)	-0.34(-0.68, 0.00)	41	-0.14(-0.32, 0.04)	-0.47(-0.65, -0.29)	71	-0.23(-0.36, -0.10)	-0.67(-0.81, -0.54)
12	-0.17(-0.42, 0.07)	-0.45(-0.70, -0.20)	42	0.00(-0.18, 0.18)	-0.21(-0.38, -0.04)	72	0.07(0.01, 0.14)	-0.31(-0.37, -0.24)
13	-0.27(-0.57, 0.04)	-0.98(-1.00, -0.59)	43	-0.23(-0.47, 0.01)	-0.25(-0.50, 0.00)	73	-0.38(-0.65, -0.12)	-0.69(-0.99, -0.38)
14	-0.08(-0.23, 0.06)	-0.49(-0.62, -0.35)	44	-0.35(-0.55, -0.15)	-0.22(-0.43, -0.01)	74	-0.27(-0.46, -0.07)	-1.00(-1.00, -0.80)
15	-0.50(-0.86, -0.14)	-0.29(-0.68, 0.09)	45	-0.12(-0.33, 0.10)	-0.08(-0.31, 0.14)	75	-0.37(-0.59, -0.16)	-0.66(-0.90, -0.43)
16	-1.00(-1.00, -0.94)	-1.00(-1.00, -0.93)	46	0.00(-0.87, 0.87)	0.24(-0.36, 0.85)	76	-0.04(-0.23, 0.16)	-0.19(-0.38, 0.00)
17	0.00(-0.32, 0.32)	-0.22(-0.54, 0.10)	47	-0.06(-0.26, 0.15)	-0.14(-0.35, 0.06)	77	-0.42(-0.51, -0.34)	-0.63(-0.72, -0.55)
18	-0.46(-0.78, -0.14)	-0.25(-0.60, 0.09)	48	0.10(-0.37, 0.57)	-0.05(-0.62, 0.52)	78	-0.06(-0.20, 0.07)	-0.55(-0.68, -0.42)
19	-0.95(-1.00, -0.89)	-1.00(-1.00, -0.96)	49	-0.27(-0.57, 0.04)	-0.64(-0.99, -0.30)	79	0.00(-0.53, 0.52)	0.11(-0.36, 0.57)
20	0.36(0.18, 0.55)	-0.08(-0.40, 0.25)	50	-0.01(-0.38, 0.36)	-0.92(-1.00, -0.47)	80	0.37(-0.10, 0.85)	-0.09(-0.99, 0.82)
21	-0.62(-0.90, -0.33)	-0.44(-0.74, -0.14)	51	0.15(-0.22, 0.52)	0.13(-0.27, 0.52)	81	0.50(0.21, 0.79)	0.24(-0.21, 0.70)
22	-0.05(-0.21, 0.11)	-0.05(-0.21, 0.12)	52	-1.00(-1.00, -0.94)	-1.00(-1.00, -0.92)	82	0.82(0.79, 0.85)	0.83(0.80, 0.86)
23	-0.53(-0.80, -0.27)	-0.24(-0.52, 0.04)	53	-0.10(-0.21, 0.02)	-0.48(-0.59, -0.37)	83	1.00(-1.00, 1.00)	1.00(0.68, 1.00)
24	-0.21(-0.35, -0.07)	-0.48(-0.61, -0.34)	54	-0.41(-0.77, -0.05)	-0.42(-0.81, -0.02)	84	0.15(-0.14, 0.45)	-0.05(-0.44, 0.34)
25	-0.44(-0.70, -0.17)	-0.31(-0.59, -0.03)	55	0.48(-0.09, 1.00)	0.45(-0.16, 1.00)	85	0.05(-0.24, 0.33)	-0.98(-1.00, -0.63)
26	-0.04(-0.31, 0.22)	-0.28(-0.54, -0.01)	56	0.00(-0.55, 0.54)	-0.05(-0.61, 0.52)	86	-0.35(-0.74, 0.04)	-0.69(-1.00, -0.20)
27	0.17(0.07, 0.28)	-0.08(-0.21, 0.06)	57	0.03(-0.19, 0.25)	-0.26(-0.49, -0.03)	87	-0.74(-1.00, 0.15)	0.29(-0.24, 0.82)
28	-0.26(-0.45, -0.07)	-0.47(-0.66, -0.27)	58	0.35(0.04, 0.67)	-0.04(-0.61, 0.52)	88	0.53(0.19, 0.87)	0.20(-0.41, 0.80)
29	-0.28(-0.55, -0.01)	-0.69(-0.99, -0.40)	59	0.00(-0.42, 0.42)	-0.71(-1.00, -0.23)	89	0.04(-0.20, 0.29)	-0.89(-1.00, -0.55)
30	0.00(-0.29, 0.28)	-0.30(-0.58, -0.03)	60	-0.12(-0.66, 0.41)	-0.05(-0.62, 0.52)	90	0.89(0.65, 1.00)	0.86(0.54, 1.00)
31	0.13(-0.21, 0.47)	-0.12(-0.54, 0.30)	61	-0.44(-0.58, -0.31)	-0.56(-0.70, -0.43)

NOTE.—Table 2 is also available in machine-readable form in the electronic edition of the *Astrophysical Journal*.
^a Sources 7 and 10 are very close together, and we report their combined hardness ratios.

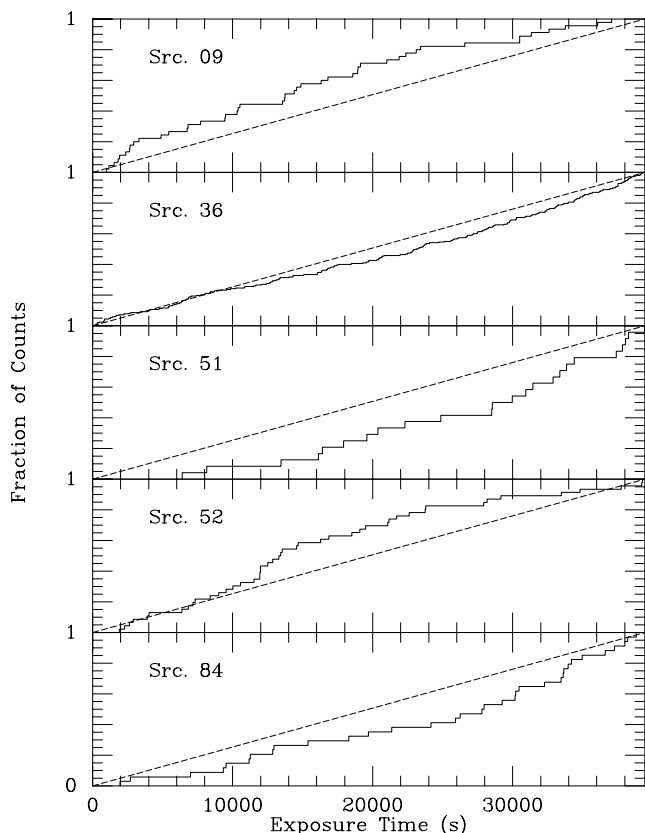


FIG. 4.—Solid histogram gives the accumulated fraction of events for sources as a function of the accumulated exposure time. The dashed line is the predicted distribution under the hypothesis that the source plus background rate is constant. The five sources shown are those with more than 20 net counts (subtracting background) and with variability detected at greater than 95% confidence.

within 3.5 of the center of NGC 4697, which is slightly less than the distance to the nearest chip edge.

Figure 5 shows the distribution of the absolute values of the P.A. of the sources. Here P.A. is measured from north to east and is taken to be in the range $-180^\circ < \text{P.A.} \leq 180^\circ$. For a set of sources whose projected density is constant on concentric aligned ellipses of constant ellipticity e , the distribution of angles ϕ relative to the semimajor axis is

$$n(\phi)d\phi = \frac{N(1-e)}{2\pi} \frac{d\phi}{(1-e)^2 \cos^2 \phi + \sin^2 \phi}, \quad (2)$$

where $n(\phi)d\phi$ is the number of sources with angles between ϕ and $\phi + d\phi$ and N is the total number of sources. The short-dashed curve in Figure 5 is the predicted distribution based on the optical photometry of the galaxy, plus the expected number of background sources in this region. The optical photometry gives $\text{P.A.} = 67^\circ \pm 4^\circ$ and $e = 0.42 \pm 0.06$ (Jedrzejewski et al. 1987; Faber et al. 1989; Peletier et al. 1990); the errors approximately cover the range of values in the literature plus the radial variation at radii greater than $10''$. The long-dashed curve is the best-fit elliptical distribution plus background, determined by a maximum likelihood fit to the observed values. The best-fit distribution gives $\text{P.A.} = 79^\circ \pm 15^\circ$ and $e = 0.40 \pm 0.09$. The best-fit curve is not a statistically significant improvement on the optical model.

We also compared the radial distribution of sources with the photometry of the optical light. Figure 6 shows the

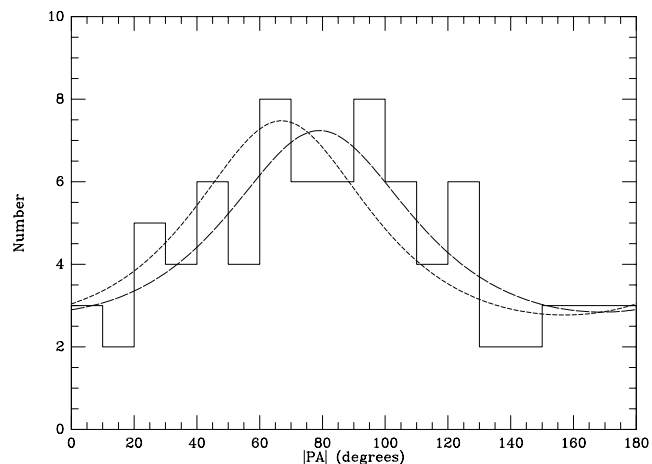


FIG. 5.—Solid histogram gives the distribution of the position angles of the X-ray sources within 3.5 of the center of NGC 4697 in 10° bins, as a function of the absolute value of the P.A. P.A. is measured from north to east and is taken to be in the range $-180^\circ < \text{P.A.} \leq 180^\circ$. The short-dashed curve is the predicted distribution based on the optical photometry of the galaxy, plus the expected number of background sources in this region. The long-dashed curve is the best-fit elliptical distribution plus background, determined by a maximum likelihood fit to the observed values.

accumulated source number as a function of the radius. The dashed curve is the predicted distribution if the source counts follow the optical light in the galaxy plus the expected number of background sources. The optical photometry was modeled as a de Vaucouleurs profile with effective semimajor and semiminor axes of $a_{\text{eff}} = 95''$ and $b_{\text{eff}} = 55''$. The K-S test indicates that the optical distribution is a good fit to the X-ray source distribution. We determined the best-fit de Vaucouleurs profile plus background fit to the source radial distribution, but it was not distinguishable from the optical distribution. We also did this analysis using the elliptical semimajor axes of the sources (a values in Table 1), but the results were nearly identical. These comparisons show that the X-ray source distribution is elongated in about the same direction and by about the same amount as the optical light and that the radial distribution

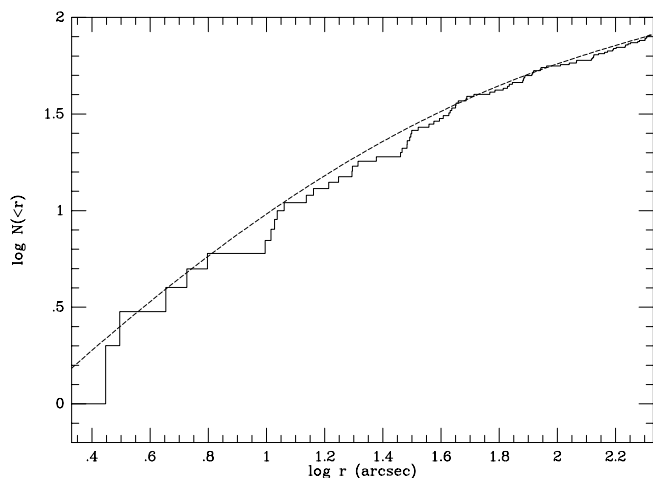


FIG. 6.—Solid histogram gives the accumulated number of X-ray sources within 3.5 of the center of NGC 4697 as a function of the radius. The dashed curve is the predicted distribution based on the optical photometry of the galaxy, plus the expected number of background sources in this region.

of X-ray sources is proportional to that of the optical light, all to within the errors.

5. DIFFUSE EMISSION

5.1. Resolved versus Diffuse Emission

We determined the portion of the X-ray emission due to resolved sources and unresolved emission, both for the entire *Chandra* X-ray band (0.3–10 keV) and for three narrower bands: hard (2–10 keV), medium (1–2 keV), and soft (0.3–1 keV). We found that these bands gave reasonable count rates and spectral discrimination for a spectrum like that of the entire galaxy (§ 6), which has very soft and very hard components. The emission was determined for two spatial regions. First, it was done within the elliptical optical isophote that contains one-half of the optical light from the galaxy. We refer to these counts as coming from within “one effective radius.” This isophote has an effective semimajor axis of $95''$, an effective semiminor axis of $55''$, an ellipticity of 0.42, and a P.A. of 67° . We also determined the fluxes within an elliptical annular region ranging from one to two effective radii. The population of resolved sources was determined as discussed above (§ 4). Then, the total emission was determined and the source flux subtracted to give the amount of unresolved emission.

The results are listed in Table 3. For each spatial region, the emission is divided into “Resolved” and “Unresolved” components, with “All” denoting the sum of these two. The truly “Diffuse” emission is the unresolved emission, corrected for unresolved binary sources (§ 5.2), while “Discrete” emission is the sum of resolved and unresolved binary sources. The emission is divided into the soft (*S*), medium (*M*), and hard (*H*) bands, with “Total” denoting the sum of these (all emission from 0.3 to 10 keV). In addition to the total number of counts, we give the hardness ratios H21 and H31 as defined in § 4.4. The fractional contribution of resolved, unresolved, and truly diffuse emission to the counts within each band is given. Finally, the unabsorbed luminosity for each component and band is given, based on the best-fit spectra for each component (§ 6 and Table 4).

Within one effective radius, 61% of the counts and 71% of the X-ray luminosity is resolved into individual X-ray sources for the total band. In the hard, medium, and soft bands, the resolved count fractions are 81%, 79%, and 48%, respectively. Between one and two effective radii, the resolved fraction drops but the spectrum of the unresolved emission gets harder, suggesting that this is partly the result of lower sensitivity to point sources at radii where the PSF

TABLE 3
RESOLVED VERSUS DIFFUSE EMISSION

Region	Origin	Band	Counts	Hardness (H21 or H31)	Fraction (%)	Luminosity (10^{40} ergs s^{-1})
$<1a_{\text{eff}}$	All	Total	3715 ± 90	...	(100)	1.57
		<i>H</i>	584 ± 69	$-0.57^{+0.04}_{-0.04}$	(100)	
		<i>M</i>	975 ± 36	$-0.38^{+0.03}_{-0.03}$	(100)	
		<i>S</i>	2154 ± 107	...	(100)	
	Resolved	Total	2271 ± 57	...	61 ± 10	1.11
		<i>H</i>	474 ± 31	$-0.37^{+0.03}_{-0.03}$	81 ± 14	
		<i>M</i>	771 ± 35	$-0.14^{+0.03}_{-0.03}$	79 ± 5	
		<i>S</i>	1026 ± 41	...	48 ± 3	
	Unresolved	Total	1444 ± 107	...	39 ± 10	0.46
		<i>H</i>	110 ± 76	$-0.82^{+0.15}_{-0.09}$	19 ± 14	
		<i>M</i>	204 ± 50	$-0.69^{+0.08}_{-0.06}$	21 ± 5	
		<i>S</i>	1128 ± 115	...	52 ± 3	
	Diffuse	Total	869 ± 138	...	23 ± 4	0.18
		<i>S</i>	869 ± 138	...	40 ± 7	
	Discrete	Total	2846 ± 166	...	77 ± 4	1.39
		<i>H</i>	584 ± 69	(-0.37)	(100)	
<i>M</i>		975 ± 36	(-0.14)	(100)		
<i>S</i>		1285 ± 85	...	60 ± 7		
$1a_{\text{eff}}-2a_{\text{eff}}$	All	Total	1831 ± 107	...	(100)	0.65
		<i>H</i>	92 ± 223	$-0.88^{+0.71}_{-0.11}$	(100)	
		<i>M</i>	247 ± 33	$-0.72^{+0.06}_{-0.05}$	(100)	
		<i>S</i>	1492 ± 269	...	(100)	
	Resolved	Total	365 ± 25	...	19 ± 2	0.18
		<i>H</i>	68 ± 14	$-0.44^{+0.10}_{-0.09}$	>48	
		<i>M</i>	125 ± 16	$-0.16^{+0.08}_{-0.08}$	51 ± 9	
		<i>S</i>	173 ± 18	...	12 ± 2	
	Unresolved	Total	1466 ± 110	...	81 ± 2	0.47
		<i>H</i>	24 ± 223	$-0.96^{+1.95}_{-0.04}$	<52	
		<i>M</i>	122 ± 37	$-0.83^{+0.07}_{-0.05}$	49 ± 9	
		<i>S</i>	1319 ± 270	...	88 ± 2	
	Diffuse	Total	1110 ± 163	...	61 ± 10	0.30
		<i>S</i>	1110 ± 163	...	74 ± 17	
	Discrete	Total	721 ± 127	...	39 ± 10	0.35
		<i>H</i>	92 ± 223	(-0.88)	(100)	
<i>M</i>		247 ± 33	(-0.72)	(100)		
<i>S</i>		382 ± 68	...	26 ± 17		

is larger. However, it is also clear that there is a very spatially extended soft component to the X-ray emission.

5.2. Unresolved Binary Sources and Truly Diffuse Emission

A portion of the unresolved emission must also come from LMXBs that fall below our threshold for reliable detection of resolved sources. Indeed, if one sets the detection threshold for sources lower, one finds many more 2σ fluctuations than expected just from Poisson statistics. However, it would be difficult to use such a fluctuation analysis to extend the statistical detection of LMXBs down a factor of ~ 50 to $L_X \sim 10^{36}$ ergs s^{-1} , the approximate lower limit for LMXBs in globular clusters (Hertz & Grindlay 1983). If the observed luminosity function of the resolved sources in NGC 4697 (Fig. 4, Paper I) is extended down to $L_X = 10^{36}$ ergs s^{-1} , the contribution of LMXBs to the total band X-ray emission from NGC 4697 increases by about 17%. This result agrees approximately with the result from the X-ray colors of the sources and unresolved emission given in the next paragraph. Still, this is a rather significant extrapolation, which could be inaccurate if the slope of the luminosity function changes below $L_X = 5 \times 10^{37}$ ergs s^{-1} , as is seen in the bulge of M31 (Shirey et al. 2001).

We have estimated the portion of the unresolved emission that is due to unresolved LMXBs based on the X-ray hardness ratios of the sources. The spectral analysis (§ 6) indicates that LMXBs produce the majority of the X-ray luminosity at photon energies above 1 keV. Thus, we assume that all of the hard (H) and medium (M) counts in the unresolved emission come from unresolved discrete sources. Moreover, we assume that these unresolved sources have the same spectral properties as the resolved sources. We use the hardness ratios of the resolved sources and the $H + M$ counts of the unresolved emission to correct the soft (S) band unresolved emission for unresolved LMXBs. The counts and fractions for this truly “Diffuse” component are listed in Table 3. When corrected in this way, it appears that LMXBs (resolved and unresolved) provide 77% of the total band counts and 89% of the luminosity in the inner effective radius.

The X-ray spectrum of the unresolved emission consists of two components: a hard component with a spectrum that is consistent with that of the resolved sources, and a soft component (§ 6.2). If we attribute the hard component to unresolved sources, then we can determine the total luminosity of the discrete sources from the luminosity of the hard component in the total spectrum (§ 6). Based on the spectral fits, we would conclude that 74% of the total luminosity is due to discrete sources. The differences in the results using colors or spectral fits partly reflect uncertainties in the spectral fits and count rates and differences in the spectral models of the different components. However, this difference may also be due to errors in the calibration of the ACIS S3 below 0.7 keV (§ 6). As a result of concerns about the low-energy spectral calibration, we use the hardness ratios and counts rather than spectra to determine the portion of the unresolved emission that is due to LMXBs. Using the spectra requires extrapolating the fit for the spectral range 0.7–10 keV down to 0.3 keV, where the spectral calibration appears to be very uncertain. Using the hardness ratios involves only assuming that the unresolved LMXBs have the same spectrum as resolved sources.

The remaining $\sim 11\%$ of the luminosity and $\sim 23\%$ of the counts would come from a more diffuse component with

a soft (~ 0.3 keV) spectrum. In § 7.3 we show that this emission is almost certainly due to diffuse gas.

5.3. Spatial Distribution of Diffuse Emission

We determined the radial distribution of the diffuse emission. Because we are mainly interested in the (presumably gaseous) soft component, we did this in the soft band (0.3–1.0 keV). Resolved sources were excluded. The unresolved emission was collected in circular annuli. (We also determined the surface brightness in elliptical annuli whose orientation and ellipticity matched that of the optical isophotes of the galaxy, and the results were essentially identical to those for circular annuli.) The outer boundary of the largest annulus was the largest circle that fitted entirely on the S3 chip; thus, regions of the chip corners, south edge, and west edge were not used to determine the surface brightness. The profile was corrected for background and for exposure. As noted previously, the background at large radii is quite uncertain as a result of the foreground emission by the NPS (§ 2), and we include a large systematic error in the background because of this. As discussed in § 2, this systematic error covered the range of NPS contributions from zero to all of the emission at large radii on the S3 chip. Thus, the errors in the resulting surface brightness values and model fit parameters should include the full range of possible background contributions.

The observed profile is shown in Figure 7 as a function of the projected radius r . The observed soft X-ray profile is much broader than the optical profile for the galaxy. The short-dashed line shows a de Vaucouleurs profile with an effective radius of $r_{\text{eff}} = 72''$, which is the azimuthally averaged value for the optical light. A fit to the profile with the X-ray surface brightness proportional to the optical surface brightness is completely unacceptable. We tried to fit the profile using the standard beta model

$$I_X(a) = I_0 \left[1 + \left(\frac{r}{r_c} \right)^2 \right]^{-3\beta+1/2}, \quad (3)$$

where r_c is the core radius. This provided an acceptable fit, which is shown as the long-dashed curve in Figure 7. The value of $\beta = 0.335 \pm 0.004$ implies a rather flat profile,

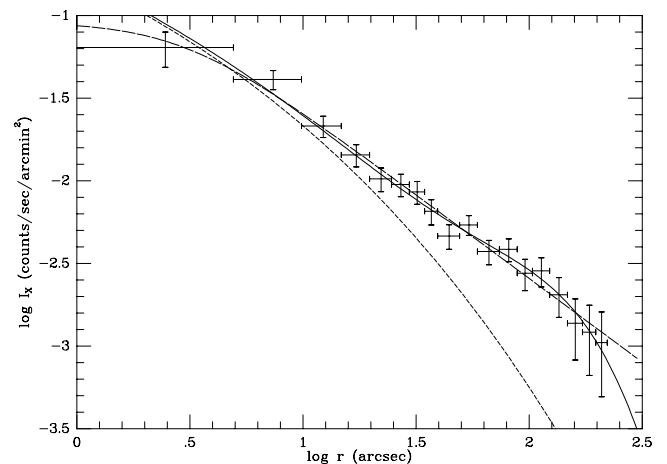


FIG. 7.—Profile of the unresolved, soft-band (0.3–1 keV) emission as a function of the projected radius r . The short-dashed curve shows a de Vaucouleurs profile that fits the optical surface brightness of the galaxy. The long-dashed curve is a beta model fit, while the solid curve is the best fit assuming that the emission is the sum of emission that is proportional to the optical light plus a beta model.

although fairly flat profiles are found in many X-ray bright elliptical galaxies (e.g., Forman et al. 1985; Trinchieri et al. 1986). On the other hand, the core radius is required to be very small, $r_c = 2''.9 \pm 0''.2$. This implies that the X-ray surface brightness is nearly a power-law function of the radius, $I_X \propto r^{-1.01}$.

The spectrum and colors of the unresolved emission indicate that a portion of this emission is due to unresolved stellar sources. The very small value of the core radius in the beta model fit also suggests that the emission near the center may have a significant contribution from unresolved stellar sources with a cuspy de Vaucouleurs profile. Thus, we also tried fitting the surface brightness profile with the sum of a de Vaucouleurs profile and beta model, with the effective radius of the de Vaucouleurs profile fixed by the optical profile as before. This led to a fit that was only marginally better than the single beta model ($\Delta\chi^2 = -1.10$ for one additional fitting parameters), shown as the solid curve in Figure 7. The normalizations of the two components are roughly consistent with the decomposition of the unresolved emission into truly diffuse and discrete emission in Table 3 in the various regions based on X-ray colors. In this fit, the values of r_c and β are both very large and poorly constrained, $r_c > 296''$ and $\beta > 1.24$. Obviously, these values are poorly determined since the core radius is larger than the largest radius at which the surface brightness is determined. This suggests a rather flat surface brightness distribution for the truly diffuse emission out to a large radius. On the other hand, a constant surface brightness is not an acceptable fit for the truly diffuse emission ($\Delta\chi^2 = 12.85$ for two fewer fitting parameters). The surface brightness due to diffuse emission is fitted acceptably with a fairly flat power-law distribution with $I_X \propto r^{-0.55}$.

In conclusion, the surface brightness distribution of the diffuse emission is uncertain because of corrections for the unresolved point sources and the background including the NPS. However, it has a radially declining surface brightness that is considerably flatter than that of the optical stellar emission from the galaxy. Note that this is true even if the diffuse emission is not corrected for the unresolved point sources (Fig. 7) and that the very extended emission occurs at surface brightness levels that exceed those of the background and the NPS by approximately 1 order of magnitude.

6. SPECTRAL ANALYSIS

At the time when this analysis was done, there were considerable uncertainties in the soft X-ray spectral response of the S3 chip below 0.7 keV (e.g., Markevitch et al. 2000). We found significant residual deviations in most of the spectral fits for any reasonable spectrum at energies $\lesssim 0.7$ keV. In addition, we have previously determined the spectrum of NGC 4697 with both the *ROSAT* PSPC and *ASCA* (ISB00). We found that the *Chandra* spectrum at low energies was inconsistent with the *ROSAT* PSPC or the joint *ROSAT* and *ASCA* spectra. In addition to the spectra presented in ISB00, we extracted the total *ROSAT* PSPC spectrum for the inner effective radius for comparison to the equivalent *Chandra* S3 spectrum for exactly the same region (§ 6.1). (We could not determine the *ASCA* spectrum of the same region as it is smaller than the spatial resolution of *ASCA*.) The *Chandra* and *ROSAT* spectra were completely inconsistent at soft X-ray energies; they agree very well above 0.71 keV and very poorly below this energy. Thus, we

restrict all of our spectral analysis to the energy range 0.72–10.0 keV. In order to allow χ^2 statistics to be used, all of the spectra were grouped to at least 20 counts per spectral bin.

Previous *ROSAT* and *ASCA* spectra of early-type galaxies have indicated that they have at least two spectral components: a very hard component that may be due to X-ray binaries and/or an AGN (Matsumoto et al. 1997; Allen et al. 2000), and a softer component. In X-ray luminous early-type galaxies, the soft component is dominant, and it is clearly due to diffuse gas at a temperature of ~ 1 keV (Forman et al. 1985; Canizares et al. 1987). In X-ray faint early-type galaxies, the soft component is much softer, and its origin is still uncertain (Fabbiano et al. 1994; Pellegrini 1994; Kim et al. 1996; Irwin & Sarazin 1998a, 1998b). The *ASCA* spectrum of the hard component has generally been fitted either by a power law (characterized by a photon spectral index Γ , where $\Gamma > 0$ implies a photon spectrum that declines with energy; Allen et al. 2000) or by a thermal bremsstrahlung spectrum (characterized by a hard component temperature T_h ; Matsumoto et al. 1997). The soft component in X-ray bright galaxies is usually fitted by the MEKAL model for the emission from a low-density, optically thin plasma (Irwin & Sarazin 1998a, 1998b). This model is characterized by the temperature of the gas (T_s) and by the abundances of the heavy elements. Given the limited statistics we have in our spectra, we will assume that the heavy-element abundances have the solar ratios and only allow the overall abundance of the heavy elements to vary. In X-ray faint galaxies, it is unclear what the appropriate soft emission model should be. If the soft emission is due to diffuse gas, then the MEKAL model would again be appropriate. If it is due to an optically thick stellar component (including the same LMXBs that produce the hard component), then it might be better represented as a blackbody, characterized by a temperature (T_s again). Thus, we have used spectral models that include both a hard (power law or bremsstrahlung) and soft (MEKAL or blackbody) component. In ISB00, the spectrum of NGC 4697 was fitted with the sum of a hard bremsstrahlung and soft MEKAL model.

Models were fitted to the spectra using XSPEC. The results are summarized in Table 4, where the errors are at the 90% confidence level. This table gives the absorbing column N_H , hard spectral model, bremsstrahlung temperature T_h or power-law photon index Γ , unabsorbed flux of the hard component F_X^h (0.3–10 keV), soft component model, soft component temperature T_s , abundance (relative to solar) for the MEKAL component, unabsorbed flux of the soft component F_X^s (0.3–10 keV), number of net counts in the spectrum, and χ^2 per degree of freedom (dof). The Galactic absorbing column toward NGC 4697 is $N_H = 2.12 \times 10^{20} \text{ cm}^{-2}$ (Stark et al. 1992).

6.1. X-Ray Spectra of Resolved Sources

The background for the resolved sources came from regions located around each source with 3 times the area of the regions for the source spectrum. We first determined the X-ray spectrum of all of the resolved sources within one effective radius. The resulting spectrum, which gave about 1600 counts in the 0.72–10 keV energy range after subtraction of background, is shown in Figure 8.

We first fitted the spectrum assuming the same spectral properties and properties as were used to fit the total *ASCA* plus *ROSAT* spectrum in ISB00 (row 1, Table 4). The nor-

TABLE 4
X-RAY SPECTRAL FITS

Row	Origin	Region	N_H (10^{20} cm $^{-2}$)	HARD COMPONENT			SOFT COMPONENT				χ^2/dof	
				Model	kT_h or Γ (keV)	F_X^h (0.3–10 keV) (10^{-13} ergs cm $^{-2}$ s $^{-1}$)	Model	kT_s or kT_{bb} (keV)	Abund.	F_X^s (0.3–10 keV) (10^{-13} ergs cm $^{-2}$ s $^{-1}$)		Counts
1	Sources	$< 1a_{\text{eff}}$	(2.12)	Brems	(5.2)	3.11 ± 0.17	MEKAL	(0.26)	(0.07)	< 0.11	1595	60.1/70
2	Sources	$< 1a_{\text{eff}}$	(2.12)	Brems	(5.2)	3.11 ± 0.14				(0.0)	1595	60.1/71
3 ^a	Sources	$< 1a_{\text{eff}}$	(2.12)	Brems	$8.1^{+2.8}_{-1.9}$	3.50 ± 0.15				(0.0)	1595	51.4/70
4	Sources	$< 1a_{\text{eff}}$	< 3.90	Brems	$9.1^{+3.5}_{-2.5}$	3.49 ± 0.15				(0.0)	1595	50.3/69
5	Sources	$< 1a_{\text{eff}}$	(2.12)	Power	1.57 ± 0.08	3.96 ± 0.23				(0.0)	1595	52.9/70
6	Sources	$< 1a_{\text{eff}}$	(2.12)	Brems	$9.3^{+5.0}_{-2.5}$	3.53 ± 0.19	bbody	< 1.70		< 0.42	1595	48.8/68
7	Sources	$> 1a_{\text{eff}}$	(2.12)	Brems	(8.1)	3.39 ± 0.07				(0.0)	1586	99.8/70
8	Sources	$> 1a_{\text{eff}}$	(2.12)	Brems	30^{+39}_{-13}	4.42 ± 0.69				(0.0)	1586	74.5/69
9 ^a	Sources	$> 1a_{\text{eff}}$	14.2 ± 5.6	Brems	$9.7^{+6.7}_{-3.0}$	4.38 ± 0.33				(0.0)	1586	61.8/68
10	Sources	$L_X < L_b$	(2.12)	Brems	$6.5^{+3.3}_{-3.0}$	1.89 ± 0.12				(0.0)	908	37.0/44
11 ^a	Sources	$L_X < L_b$	(2.12)	Brems	$10.8^{+28.7}_{-4.7}$	1.93 ± 0.19	bbody	$0.14^{+0.10}_{-0.04}$		$0.21^{+0.48}_{-0.21}$	908	30.8/42
12	Sources	$L_X > L_b$	(2.12)	Brems	$9.1^{+4.9}_{-2.6}$	2.03 ± 0.12				(0.0)	906	40.2/40
13 ^a	Sources	$L_X > L_b$	$9.0^{+7.9}_{-1.1}$	Brems	$6.4^{+4.2}_{-2.1}$	2.03 ± 0.30				(0.0)	906	38.3/39
14	Unresolved	$< 1a_{\text{eff}}$	(2.12)	Brems	(5.20)	$0.39^{+0.07}_{-0.23}$	MEKAL	(0.26)	(0.07)	1.19 ± 0.18	705	79.9/105
15	Unresolved	$< 1a_{\text{eff}}$	< 22.83	Brems	(5.20)	$0.29^{+0.14}_{-0.17}$	MEKAL	(0.26)	(0.07)	$1.52^{+1.18}_{-0.36}$	705	78.5/104
16	Unresolved	$< 1a_{\text{eff}}$	(2.12)	Brems	$1.5^{+24.9}_{-1.0}$	$0.29^{+0.99}_{-0.22}$				$1.12^{+0.22}_{-0.22}$	705	77.5/102
17 ^a	Unresolved	$< 1a_{\text{eff}}$	(2.12)	Brems	(8.1)	$0.27^{+0.22}_{-0.21}$	MEKAL	$0.29^{+0.10}_{-0.07}$	> 0.03	$1.16^{+0.08}_{-0.13}$	705	79.4/103
18 ^a	Total	$< 1a_{\text{eff}}$	(2.12)	Brems	(5.20)	(3.45)	MEKAL	(0.26)	(0.07)	(1.22)	2372	135.0/156
19	Total	$< 1a_{\text{eff}}$	< 3.07	Brems	(5.20)	(3.45)	MEKAL	(0.26)	(0.07)	(1.22)	2372	134.4/155
20	Total	$< 1a_{\text{eff}}$	(2.12)	Brems	$5.7^{+2.6}_{-1.5}$	3.62 ± 0.26	MEKAL	$0.22^{+0.09}_{-0.04}$	> 0.02	1.46 ± 0.31	2372	131.4/151
21	Total	$1a_{\text{eff}} - 2a_{\text{eff}}$	(2.12)	Brems	(8.1)	$0.38^{+1.09}_{-0.21}$	MEKAL	$0.26^{+0.13}_{-0.06}$	(0.07)	$1.78^{+0.49}_{-1.01}$	817	193.7/243

^a The adopted best-fit model for this emission.

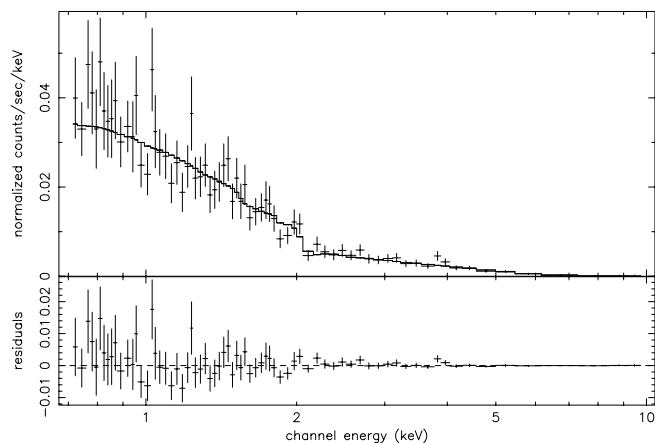


FIG. 8.—Data points in the upper panel are the cumulative X-ray spectrum of all of the resolved sources in the inner effective radius of NGC 4697. The solid histogram is the best-fit model spectrum (row 3, Table 4). The lower panel shows the residuals to the fit.

malizations of the hard (bremsstrahlung) and soft (MEKAL) components were allowed to vary. This gave a good fit to the spectrum of the sources, but the flux of the soft component was very weak; the fit only gave an upper limit that was much lower than the hard flux. Thus, we tried removing the soft component completely in the fit (row 2). This gave a fit that was just as good ($\Delta\chi^2 < 0.001$) with one less free parameter. Thus, we conclude that, on average, the resolved sources in NGC 4697 have no soft component to their spectra and that any soft component in the overall galaxy spectrum must come from a distinct, unresolved component, such as interstellar gas.

Next, we allowed the temperature T_h of the hard component to vary (row 3). This resulted in a somewhat higher temperature than had been given by the total *ASCA* plus *ROSAT* spectrum, which did not resolve the spectra of the sources separately. The new fit was a considerable improvement, with $\Delta\chi^2 = 8.7$ for only one more free parameter, which is significant at the 99.9% level according to the *F*-test. We will adopt this as our best-fit model for the resolved source population within the inner effective radius. This fit is shown with the data in Figure 8. Since this region combines good statistics with a high probability that the sources are associated with NGC 4697, we will also use this fit as our standard model for the spectrum of the LMXB population of NGC 4697.

Next, we allowed the absorbing column to vary to see if there was evidence of any excess absorption beyond the Galactic column (row 4). We can only give an upper limit to the absorbing column, which is somewhat greater than the Galactic value. Presumably, this is partly due to removing the softest energies from the spectra due to the calibration uncertainties discussed above. Since allowing the absorbing column to vary did not result in a greatly improved fit ($\Delta\chi^2 = 1.1$ for one more free parameter), we will fix the absorption at the Galactic value.

Finally, we considered different models for the hard and soft components. We represented the hard component by a power law rather than by bremsstrahlung (row 5). This resulted in a slightly worse fit than with bremsstrahlung, so we will use the bremsstrahlung model for the hard component due to LMXBs. Then, we tried using a blackbody model for the soft component. This produced a better fit

than the MEKAL model, but still no soft component was required at the 90% confidence level.

We also determined the cumulative X-ray spectrum of the resolved sources outside of one effective radius (rows 7–9). As was true of the inner sources, these spectra are well fitted without any soft component in the spectrum. The cumulative spectrum of the outer sources is considerably harder than that of the inner sources and is fitted best with an absorbing column that is much higher than Galactic (row 9). In row 7, we give the results of fitting the spectrum of the outer sources using the same spectral parameters as fit the inner sources (row 3). This did not provide a very good fit. Rows 8 and 9 show the result of freeing the hard component temperature T_h and the absorbing column. The inner source spectral model can be rejected with very high confidence ($\geq 99\%$). We believe that this difference is mainly due to the greater influence of background sources in the outer regions of the S3 chip. Many of the background sources have hardness ratios that indicate that they have very hard, strongly absorbed spectra (§ 4.4; Fig. 4 in Paper I). For example, source 82 is the brightest X-ray source on the S3 chip and provides about one-quarter of the counts in the spectrum of outer sources. It has a very hard, strongly absorbed spectrum.

We also tried to fit the spectra of the brightest and faintest sources separately (rows 10–13). Because the luminosity function shows a break at a characteristic luminosity L_b , we separated sources into brighter sources ($L_x > L_b$) and fainter sources ($L_x < L_b$). In order to include as many sources as possible to improve the statistics but avoid too many background sources, we considered all sources within an elliptical optical isophote with a semimajor axis of $2a_{\text{eff}}$. For the fainter sources, the best-fit spectra were consistent with the Galactic column, so we fixed the absorption at this level. Unlike the case for the integrated spectra of all the sources within one effective radius, the spectral fit was improved significantly by including a soft component. Either a MEKAL or blackbody spectrum did almost exactly as well. However, the abundance in the MEKAL model was essentially unconstrained, and there is no clear evidence for emission lines in the spectrum, so we adopt a blackbody model for the soft component. Rows 10 and 11 of Table 4 show the fits without and with the soft component. The flux of the soft component is small, but it improves the fit significantly. The spectra of the brighter sources did not require any soft component. On the other hand, they have a higher absorbing column and a lower bremsstrahlung temperature. The net effect is that the fainter sources may have more very soft emission, while the brighter sources have more emission at 1–2 keV.

6.2. X-Ray Spectra of Unresolved Emission

We also determined the X-ray spectra of the unresolved emission in NGC 4697. Because the unresolved emission has a low surface brightness and the background is high and uncertain as a result of the superposed NPS (§ 2), we were only able to extract a useful spectrum for the central portion of the unresolved emission. Thus, we will only consider the unresolved X-ray spectrum from within the inner effective radius; even in this region, the net counts in the spectrum after subtraction of background are only ≈ 700 , which is marginal for spectral analysis. The spectrum was extracted from the inner effective radius region, excluding small regions around each of the sources. Because the

excluded regions also contain unresolved emission, the fluxes we derive will be somewhat smaller than the total fluxes for unresolved emission in the same region (e.g., as given in Table 3). The background for this spectrum and the spectra of the total emission (§ 6.3) were taken from a combination of blank-sky and outer S3 chip spectra in order to remove the effects of the NPS, as discussed above (§ 2). We include a systematic error in the background, which means that the best-fit values of χ^2 will be somewhat smaller than expected for uncorrelated Gaussian statistical errors.

We started by fitting this spectrum with the spectrum derived from the *ROSAT* spectrum of the same region, which consisted of a bremsstrahlung hard component and a MEKAL soft component (row 14). Both the hard and soft components are required to fit the spectrum, but the hard component is fairly weak. The unresolved emission is much softer than the emission from the resolved sources. Allowing the absorbing column to vary did not improve the fit very significantly and resulted in only an upper limit on N_{H} (row 15). Thus, we will keep the column fixed at the Galactic value.

If all of the spectral parameters are allowed to vary (row 16), the fit is not significantly better, and the temperature of the hard bremsstrahlung component is nearly unconstrained. Under the assumption that the hard component is from fainter discrete sources (presumably LMXBs) with a spectrum similar to that of the resolved sources, we fix the temperature of the hard component to the value (8.1 keV) found for the resolved sources in the same region (row 3).

This fit is shown in row 17 and Figure 9. The observed spectrum shows the (mainly) Fe xvii (~ 0.72 keV emitted), Fe xvii (0.826 keV emitted) and the Ne x, Fe xvii, Fe xxi (~ 1.02 keV) line complexes, which indicates that the soft unresolved emission is due to diffuse gas. At lower energies where the spectral calibration is uncertain, the O viii line at 0.654 keV is clearly seen. Some of the line ratios in the data appear to be inconsistent with the model; for example, the Fe xvii (0.826 keV emitted) line complex is too weak in the model. This may indicate that there are calibration problems with the spectra even above 0.72 keV or that the model is incorrect in some way.

The fraction of the emission in the hard component is smaller than expected from the analysis of the X-ray colors

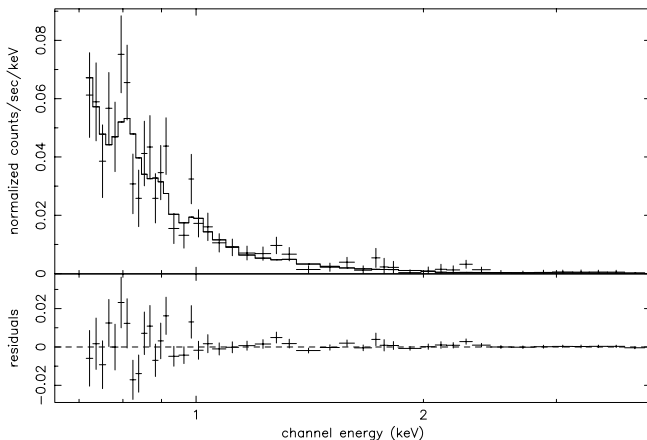


FIG. 9.—Spectrum of unresolved emission from within the inner effective radius. The notation is the same as in Fig. 8. The solid histogram is the *ROSAT* adapted spectral model for the unresolved emission (row 17, Table 4).

(Table 3) or the spatial distribution of the unresolved emission (§ 5.3). This may be the result of uncertainties in the soft X-ray spectral response of the ACIS S3 detector, as noted above. In addition, the regions used to exclude sources from the unresolved emission remove a higher fraction of the area near the center of the galaxy, and there is evidence that the unresolved emission gets softer as the radius increases.

6.3. Total X-Ray Spectra

We also determined the total (resolved and unresolved emission) X-ray spectra for various regions in NGC 4697. We first consider the total X-ray spectrum from within the inner effective radius. Initially, we fitted this spectrum using exactly the *ROSAT* spectrum (ISB00) from the same region (row 18). This model included a bremsstrahlung hard component and a MEKAL soft component. As discussed above, this gave a terrible fit if the energy range used was 0.3–10.0 keV but gave a good fit if the soft X-ray channels were dropped (for the range 0.72–10.0 keV). The observed spectrum and the *ROSAT* model fit are shown in Figure 10. We then tried freeing the normalizations of the hard and soft components but leaving the shape of the two components fixed at the *ROSAT* form. This did not improve the fit, and the normalizations were not changed significantly. We also tried allowing the absorbing column to vary (row 19); this did not improve the fit significantly, so we kept it fixed at the Galactic value. We then allowed all of the spectral parameters except N_{H} to vary (row 20); this did not provide a significantly improved fit given the five additional free parameters. Moreover, the abundance of the soft MEKAL emission was very poorly determined; since most of the soft emission in the spectrum is in lines, it is only the product of the MEKAL normalization times the abundance that is fixed by the spectrum.

As was the case with the unresolved spectrum, the total spectrum shows lines due to (mainly) O viii (0.654 keV emitted), Fe xvii (~ 0.72 keV emitted), Fe xvii (0.826 keV emitted), and the Ne x, Fe xvii, Fe xxi (~ 1.02 keV) line complex. As was true of the unresolved spectrum, the Fe xvii (0.826 keV emitted) line complex is too weak in the model. Figure 10 also shows the Si K α line at about 1.8 keV in the data but not in the model. This is a background feature produced by fluorescence in *Chandra*; its presence in

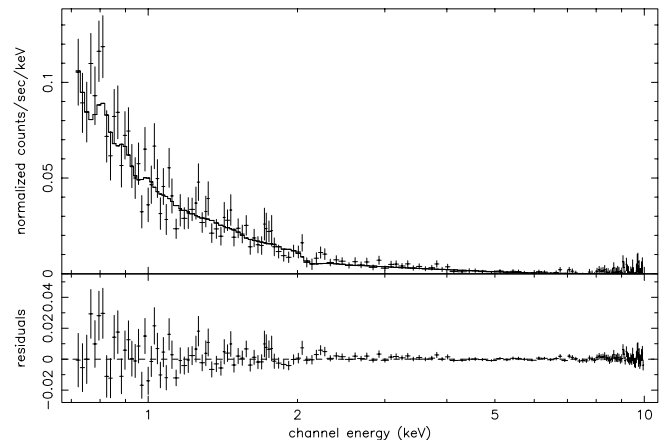


FIG. 10.—Total (sources plus unresolved emission) spectrum from within the inner effective radius. The notation is the same as in Fig. 8. The solid histogram is the *ROSAT* spectral model for the same region (row 18, Table 4).

the spectrum after subtraction of background indicates that the background subtraction is not perfect. The same feature is seen in the unresolved spectrum (Fig. 9).

At larger radii, the decreasing surface brightness of the emission, increasing contribution of the background, and the systematic uncertainty in the background make it more difficult to extract useful spectral information. We extracted the spectrum for the region from one to two effective radii (row 21). This spectrum had only about 800 net counts after correction for the background. The temperature of the hard component was not well determined but was consistent with that found for the sources in the inner region (8.1 keV), so we adopt this value. The abundance in the soft component was not well determined but consistent with the value from *ROSAT* and *ASCA* of 0.07, so we adopt this. The resulting spectral fit shows that the spectrum is more dominated by the soft emission than at smaller radii. There is no evidence for a significant temperature gradient, although the errors are large.

7. DISCUSSION

7.1. Nature of the Central Source

The position of source 1 agrees with the optical position of the center of NGC 4697 to within the combined X-ray and optical errors. This suggests that this source is actually an AGN. The luminosity of this source, $L_x = 8 \times 10^{38}$ ergs s^{-1} , is higher than most LMXBs, but there are four sources that are brighter in the S3 field. Of these, the two brightest sources in the field (sources 72 and 82) are probably background AGNs (source 72 definitely is), while the other two (sources 36 and 40) are probably LMXBs in NGC 4697. On the other hand, the hardness ratios for the central source ($H21 = -0.22^{+0.09}_{-0.09}$, $H31 = -0.34^{+0.09}_{-0.08}$) are very typical of those for the LMXBs (Table 2; Fig. 4 in Paper I), which have average hardness ratios of ($H21$, $H31$) = (-0.14, -0.37) within the inner effective radius. Thus, based on the X-ray evidence alone, the central source might be either the active nucleus in NGC 4697 or one or more LMXBs seen in projection against the nucleus. The central source appears to be slightly extended, which might indicate that it is the result of more than one point source.

NGC 4697 is not a radio source at a fairly restrictive level (Birkinshaw & Davies 1985). We were unable to find any other clear evidence for nuclear activity in the literature. This might argue that the central source is not due to an AGN.

Stellar dynamical measurements indicate that NGC 4697 has a central black hole (BH) with a mass $M_{BH} = 1.6 \times 10^8 M_\odot$, assuming our adopted distance of 15.9 Mpc (Gebhardt et al. 2000). If we take the observed X-ray luminosity of the central source to be an upper limit to the luminosity of an associated active nucleus, then the AGN luminosity is $\leq 4 \times 10^{-8}$ of the Eddington luminosity of the central BH.

7.2. The LMXB Population

7.2.1. X-Ray to Optical Luminosity Ratio of LMXBs

If one compares the discrete source (resolved and unresolved LMXBs) X-ray luminosity from within $1a_{eff}$ with the optical luminosity within the same region, one finds an X-ray-to-optical ratio for the LMXBs of $L_x(\text{LMXB}, 0.3\text{--}10 \text{ keV})/L_B = 8.1 \times 10^{29}$ ergs $s^{-1} L_{B\odot}^{-1}$. For comparison, we found a value of $L_x(\text{LMXB}, 0.3\text{--}10 \text{ keV})/L_B = 7.2 \times 10^{29}$ ergs $s^{-1} L_{B\odot}^{-1}$ in the S0 galaxy NGC 1553 (Blanton, Sarazin,

& Irwin 2001), although the systematic errors are larger in that case because the observation only samples the top of the X-ray luminosity function. *Chandra* observations of other ellipticals appear to show larger variations in the X-ray-to-optical ratio (R. Mushotzky & L. Angelini 2000, private communication). For the observed luminosity function in NGC 4697 (eq. [1]), most of the luminosity comes from sources near the break luminosity. In NGC 4697, there are only ~ 15 of these. Thus, part of the variation in the X-ray-to-optical ratios may be due to statistical fluctuations in the number of bright LMXBs or to individual temporal variations in their X-ray emission.

A recent *XMM-Newton* observation of the bulge of M31 resolves $\sim 90\%$ of the emission into LMXBs within a $5'$ radius of the center (Shirey et al. 2001). Using our spectral model to convert to our passband, and determining the optical luminosity in this region from the surface photometry of Walterbos & Kennicutt (1988), we find an X-ray-to-optical ratio of $L_x(\text{LMXB}, 0.3\text{--}10 \text{ keV})/L_B = 6.0 \times 10^{29}$ ergs $s^{-1} L_{B\odot}^{-1}$. Previously, Irwin & Sarazin (1998a) used *ROSAT* observations of the bulge of M31 (Primini, Forman, & Jones 1993; Supper et al. 1997) to determine the X-ray luminosity. Assuming that 90% of the emission is from LMXBs (based on the *XMM* result) and converting to our passband gives $L_x(\text{LMXB}, 0.3\text{--}10 \text{ keV})/L_B = 6.5 \times 10^{29}$ ergs $s^{-1} L_{B\odot}^{-1}$, in very good agreement with the *XMM* result. However, the X-ray-to-optical ratio in the bulge of M31 seems to be about 35% smaller than that in NGC 4697. This may be due to the steep luminosity function in M31, which causes there to be no very bright LMXBs (§ 7.2.2). Sources with $L_x \gtrsim L_b$ contribute much of the emission in NGC 4697.

Previous *ROSAT* observations of the bulge of the Sa galaxy NGC 1291 indicate an X-ray-to-optical ratio of $L_x(\text{LMXB}, 0.3\text{--}10 \text{ keV})/L_B = 8.9 \times 10^{29}$ ergs $s^{-1} L_{B\odot}^{-1}$ (Irwin & Sarazin 1998a), if one converts from the *ROSAT* hard band of 0.52–2.02 keV using our best-fit source spectrum. This agrees with the value for NGC 4697. We have confirmed this determination of the X-ray-to-optical ratio in NGC 1291 in a recent *Chandra* observation (J. A. Irwin, C. L. Sarazin, & J. N. Bregman 2001, in preparation). However, about 30% of the source emission in NGC 1291 comes from the very bright central point source, which is probably a central AGN. If this central point source is removed to determine the X-ray luminosity due to LMXBs, then the X-ray-to-optical ratio in NGC 1291 is similar to that in the bulge of M31 and about 50% smaller than that in NGC 4697. It appears that there are variations in the LMXB X-ray-to-optical ratios of early-type galaxies and spiral bulges.

7.2.2. Luminosity Function

The differential luminosity function of LMXBs in NGC 4697 is well fitted by a broken power law (eq. [1]) over the range of luminosities from 5×10^{37} to 10^{39} ergs s^{-1} . The break luminosity is $L_b = 3.2^{+2.0}_{-0.8} \times 10^{38}$ ergs s^{-1} , which is similar to the Eddington luminosity for spherical accretion onto a $1.4 M_\odot$ NS (2×10^{38} ergs s^{-1} for hydrogen accretion). Of course, in addition to the statistical uncertainties, the value of L_b is affected by systematic uncertainties in the distance to NGC 4697 and in the conversion from counts to luminosity. This agreement suggests that the sources with luminosities above the break luminosity are accreting BHs, while those below the break are predomi-

nantly NSs. This would imply that NGC 4697 contains $\gtrsim 15$ luminous X-ray binary systems containing BHs. If the more luminous of these systems ($L_x \sim 10^{39}$ ergs s^{-1}) are limited by the Eddington luminosity, they must contain fairly massive ($M \gtrsim 8 M_\odot$) BHs.

If the luminosity function were a broken power law that curved up rather than down (an “elbow” rather than a “knee”), the break might be due to the simple superposition of two power-law source distributions. Then, the apparent break in the luminosity function would just be the point where the two distributions crossed and would not necessarily have any physical meaning. However, such a superposition obviously cannot produce a broken power law that curves downward (a knee), as is observed in NGC 4697. This requires that there be at least two distinct source populations above and below the break luminosity.

We have found similar broken power-law luminosity functions in the S0 galaxy NGC 1553 (Blanton et al. 2001), and the bulge of the early-type spiral NGC 1291 shows a sharp break right at the Eddington break, with no bright nonnuclear sources above this break (J. A. Irwin et al. 2001, in preparation). Apparently, similar broken power laws are found to fit the LMXB populations in X-ray bright ellipticals as well (R. Mushotzky & L. Angelini 2000, private communication). In all cases, the break luminosity agrees with the Eddington luminosity of a $1.4 M_\odot$ NS, to within the errors. Thus, this appears to be a universal feature of the LMXB populations in optically luminous, old stellar systems.

In principle, this “Eddington break” luminosity could be used as a distance estimator for galaxies. Margon & Ostriker (1973) originally proposed that X-ray sources would be limited by the Eddington luminosity and that this might be useful as a distance estimator. Also, the use of the peak luminosity of X-ray bursts as a distance indicator in our Galaxy had been suggested (e.g., van Paradijs 1978), since type I bursts are also thought to be Eddington limited. The Eddington luminosity depends on very simple physics (electron scattering and gravity) and is determined solely by the mass of the accreting object and the mean mass per electron. In practice, the composition dependence resolves itself into two interesting cases, hydrogen-dominated plasmas (the usual case) or heavy-element-dominated plasmas (helium or heavier), which might occur if the donor star had lost its outer hydrogen-rich envelope. Although the physics of stellar core collapse is complex, the fact that most NSs in binaries have masses of approximately $1.4 M_\odot$ is presumably related to the Chandrasekhar mass, which is also determined only by simple quantum mechanics, gravity, and slightly by composition. Thus, the apparent universality of the break luminosity of LMXBs in early-type galaxies is understandable in terms of very simple physics.

Unfortunately, it is not possible to determine the break luminosity in an individual galaxy with great statistical accuracy because the number of bright LMXBs is very limited (about 15 in NGC 4697). For example, the statistical errors in the flux associated with the break luminosity in NGC 4697 imply that the distance could only be determined to about $\pm 20\%$ if the actual break luminosity were accurately known. Other distance estimators in current use give statistical errors of about 10% for early-type galaxies (e.g., Tonry et al. 2001). One situation where the Eddington break luminosity might be particularly useful would be in a group or cluster of galaxies, where one could determine the

total luminosity function for all of the LMXBs in the early-type galaxies and derive an average distance for the group or cluster.

Prior to *Chandra* and *XMM-Newton*, the Population II system with the best-determined LMXB X-ray luminosity function was the bulge of M31 (Primini et al. 1993; Supper et al. 1997; Garcia et al. 2000; Shirey et al. 2001). The recent *XMM-Newton* observation shows that the cumulative luminosity function of bulge sources in M31 is well fitted by a broken power law, with an exponent of -0.47 ± 0.03 for $36.2 \leq \log L_x < 37.4$ and -1.79 ± 0.26 for $37.4 \leq \log L_x < 38.1$ (Shirey et al. 2001). This applies to the 0.3–12 keV band, which is similar to the one we use (0.3–10 keV). These results are in good agreement with the luminosity function for the bulge of M31 previously determined by *ROSAT* (Primini et al. 1993; Supper et al. 1997). The brightest source in the bulge of M31 has a luminosity of $L_x \sim L_b$, so we cannot compare the upper end of the luminosity function in NGC 4697 with M31. On the other end, our source detection limit was $\log L_x \geq 37.7$, so we cannot compare to the low-luminosity end of the luminosity function of the bulge of M31. However, we can compare luminosity functions in the rather narrow range $37.7 \leq \log L_x \leq 38.07$ (0.3–10 keV). In this range, the exponent of the differential luminosity function (eq. [1]) in the bulge of M31 is $\alpha = 2.79 \pm 0.26$ (1 σ errors), while the exponent for NGC 4697 is $\alpha_l = 1.29^{+0.36}_{-0.49}$ (90% errors). Thus, the luminosity function in M31 declines much more steeply with luminosity. It seems that this rapid decline, combined with the much smaller optical luminosity of the bulge of M31, might account for the lack of brighter X-ray sources in M31.

7.2.3. Globular Clusters and LMXBs

We have identified seven X-ray sources at radii of greater than 1.5 in NGC 4697 with candidate globular clusters. Because globulars are not resolved in ground-based observations at the distance of NGC 4697, some of these candidate globulars might actually be background AGNs. Indeed, we have found that one of the candidate globular clusters (Hanes 1977; cluster 24, our source 72) is a background AGN at $z = 0.696$ (C. Mullis 2000, private communication). At present, there are no lists of globular clusters in the central regions ($\lesssim 1.5$) of NGC 4697, where the diffuse optical brightness of the galaxy makes it difficult to identify globular clusters in ground-based observations. Unfortunately, most of the X-ray sources (55 out of 90) are within 1.5, and within this region very few of these sources are expected to be unrelated to NGC 4697. A *Hubble Space Telescope* (*HST*) study to detect globular cluster candidates in the central region of NGC 4697 would be very useful.

Beyond 1.5, roughly 20% of the X-ray sources are associated with globular cluster candidates. On the other hand, the candidate globular clusters contain about 0.1% of the optical light of the galaxy in this region. Thus, the chance of an optical star being the donor in an LMXB is a factor of ~ 200 larger for stars in globular clusters than for field stars in NGC 4697. This indicates that globular clusters in this elliptical galaxy are a very hospitable environment for active compact binaries, as is true in our own Galaxy (e.g., Hertz & Grindlay 1983; White et al. 1995). This is generally believed to result from stellar dynamical interactions in globular clusters, which can produce compact binary systems.

One intriguing suggestion is that globular clusters might be the only location where very compact low-mass binaries can evolve and that all of the LMXBs in old stellar systems may have been formed in globulars (R. E. White, III, S. R. Kulkarni, & C. L. Sarazin 2001, in preparation). Of course, not all of the LMXBs are presently found in globulars, either in the bulge of our Galaxy or in NGC 4697. The field LMXBs might have been ejected from globular clusters by kick velocities resulting from supernovae, by stellar dynamical processes, or by the dissolution of the globular due to tidal effects.

Above, we have noted that there appear to be variations in the LMXB X-ray-to-optical ratio of early-type galaxies. If LMXBs all are produced in globulars, then the total luminosity of LMXBs might correlate better with the globular cluster population rather than the total optical luminosity. Since the specific frequency of globular clusters (the number per optical luminosity) varies from galaxy to galaxy, this might explain the variation in the LMXB X-ray-to-optical ratio. If one compares the globular cluster population in NGC 4697 with the bulge of M31, NGC 4697 has 8^{+7}_{-4} times as many globulars, and its specific globular cluster frequency S_N per unit optical luminosity is ~ 5 times higher (Harris 1991). The X-ray luminosity of LMXBs is about 5 times higher in NGC 4697, and the X-ray-to-optical ratio is about 1.35 times higher. Thus, the LMXB luminosity ratio is intermediate between the ratio of the optical luminosities and the ratio of the numbers of globular clusters. Obviously, there are too few galaxies with well-determined LMXB populations to allow a really meaningful test at present, but there should be many more from *Chandra* and *XMM-Newton* within the next few years. One confusing issue is the fact that the luminosity function of LMXBs also appears to vary widely (§ 7.2.2), which requires something more complex than simple scaling of the entire population with optical luminosity or globular cluster population.

In general, the specific frequency of globular clusters S_N increases from late- to early-type spirals, from spirals to S0s, from S0s to ellipticals, and from normal giant ellipticals to cDs (e.g., Harris 1991). If LMXBs all are born in globular clusters, then one might expect the specific frequency of LMXBs and their X-ray-to-optical ratio to increase in the same sequence. Already, *Chandra* observations may suggest an increase in the frequency of LMXBs in going from normal ellipticals to cDs (R. Mushotzky & L. Angelini 2000, private communication).

7.3. Interstellar Gas Emission

7.3.1. Nature of the Diffuse Emission

The unresolved X-ray emission associated with NGC 4697 appears to consist of (at least) two components: unresolved LMXBs and truly diffuse emission. The X-ray colors of the unresolved emission, its X-ray spectrum, and its spatial distribution are all consistent with this decomposition. The colors and spatial analysis indicate that $\approx 40\%$ of the counts and $\approx 61\%$ of the luminosity is due to unresolved LMXBs. A similar result is found by extrapolating the luminosity function of the LMXBs to lower luminosities. The X-ray spectrum gives a smaller fraction of unresolved LMXBs, but this might be due to the uncertain soft response of the ACIS S3 or to the varying area of the galaxy removed in order to exclude sources.

There are several arguments that indicate that the remaining truly diffuse emission is due to hot interstellar

gas. First, this emission has a much more extended radial distribution than the optical light in the galaxy (Fig. 7), which suggests that it is not from stellar sources. Second, the image of the diffuse emission (Fig. 2; see also Fig. 2 in Paper I) shows that it is somewhat irregular, with an L-shaped morphology. Such asymmetries are more easily produced in the distribution of gas (e.g., by ram pressure) than in the distribution of stellar sources. The diffuse emission is also much rounder than the highly elliptical distribution of optical light. Third, the diffuse emission is predominantly soft, with most of the emission below 1 keV. Finally, the X-ray spectrum of the unresolved emission shows low-ionization X-ray lines from ions such as O VIII and Fe XVII. This clearly implies that much of the soft emission is from an optically thin gas.

The surface brightness distribution of this soft gaseous component is very broad and flat, and the total mass does not appear to converge within the S3 field of view. As a result, it is difficult to determine the total mass of the interstellar gas. This problem is exacerbated by the foreground emission from the NPS, which adds a (presumably) fairly flat emission component at a similar temperature. However, we have estimated the mass within a spherical region with a 75" radius, which corresponds to the average effective radius. The mass of interstellar gas is about $1.8 \times 10^8 M_\odot$ within this region. This is much smaller than the masses of hot gas typically found in X-ray bright ellipticals (e.g., Forman et al. 1985). However, the total mass is probably a factor of $\gtrsim 3$ larger given the flat surface brightness distribution.

7.3.2. Origin of the Soft Component in X-Ray Faint Ellipticals

X-ray faint early-type galaxies have a very soft X-ray spectral component whose origin has been uncertain. One suggestion was that this emission came from the same LMXBs that produce the hard component (Irwin & Sarazin 1998a, 1998b). Now, the LMXBs in NGC 4697 do provide a significant part of the soft X-ray emission by simple virtue of the fact that they dominate the total emission. Certainly, some of the discrete X-ray sources in NGC 4697, the super-soft sources, do have a very soft X-ray spectral component. However, the cumulative spectrum of the sources does not show a significant soft X-ray spectral component and is well fitted by a hard thermal bremsstrahlung spectrum with a reasonably high temperature ($kT_h = 8.1$ keV; § 6.1). Similar results were found for the S0 galaxy NGC 1553 (Blanton et al. 2001). While there are still considerable uncertainties in the soft X-ray spectral response of the ACIS detectors on *Chandra*, it appears very unlikely that the LMXBs can account for the very soft spectral component seen previously with *ROSAT* in either NGC 4697 or NGC 1553. By extension, it appears that the soft emission in X-ray faint ellipticals is not primarily due to LMXBs.

The *XMM-Newton* spectra of the LMXBs in the bulge of M31 also show that, taken together, they do not have a strong soft spectral component (Shirey et al. 2001). This confirms the *ROSAT* result of Borozdin & Priedhorsky (2000), although Irwin & Bregman (1999) had reached the opposite conclusion.

The soft spectral component might also be due to fainter stellar sources such as active M stars or RS CVn binaries (e.g., Pellegrini 1994). There were strong energetic and spectral arguments against any of these sources (Pellegrini & Fabbiano 1994; Irwin & Sarazin 1998a). If the soft emission

were due to faint stellar sources, it would be expected to follow the optical distribution in NGC 4697 quite closely. In fact, the soft component is more spatially extended, rounder, and too irregular to be due to a large number of faint stellar sources (§ 5.3).

The spatial distribution of the soft diffuse emission in both NGC 4697 and NGC 1553 implies that it is due to diffuse gas. Even more importantly, its X-ray spectrum is dominated by low-ionization X-ray lines from ions like O VIII and Fe XVII. This clearly shows that the soft spectral component in these two early-type galaxies is due to diffuse interstellar gas. The recent *XMM-Newton* observation of the central bulge of M31 also shows that there is diffuse emission with an emission-line spectrum (Shirey et al. 2001). Thus, it appears that the source of the soft component in early-type galaxies is cool ($kT \approx 0.2\text{--}0.3$ keV) interstellar gas, as suggested by Pellegrini & Fabbiano (1994).

7.3.3. Physical State of the Hot Interstellar Gas

The interstellar gas in NGC 4697 is rather cool ($kT = 0.29$ keV) in comparison to X-ray bright ellipticals. A similar result was found for the S0 galaxy NGC 1553 (Blanton et al. 2001), the bulge of the Sa galaxy NGC 1291 (J. A. Irwin et al. 2001, in preparation), and the diffuse gas in the bulge of M31 (Shirey et al. 2001). NGC 4697 has a low velocity dispersion for a bright elliptical, $\sigma = 165$ km s⁻¹ (Faber et al. 1989). On the other hand, this galaxy also has a very high rotation velocity for an elliptical (Peletier et al. 1990), so the velocity dispersion may not be representative of the full depth of the galactic potential. The observed gas temperature is consistent with the temperature versus velocity dispersion ($kT\text{--}\sigma$) correlation derived from *ROSAT* observations of elliptical galaxies (Davis & White 1996), although this relationship was derived including a *ROSAT* single-temperature determination for NGC 4697 that is higher than the *Chandra* temperature of the gas (presumably because LMXBs and gas could not be separated in the *ROSAT* spectrum).

Why are the gas temperature and gas X-ray luminosity so low in NGC 4697 (and other X-ray faint ellipticals)? Pellegrini & Fabbiano (1994) argue that the low temperature is a result of a shallow gravitational potential, as indicated by the low velocity dispersion. As noted above, this is consistent with the observed temperature and σ , although the strong rotation in this galaxy implies that the gravitational potential may be considerably deeper than expected from the velocity dispersion.

What is the dynamical state of the interstellar gas in NGC 4697? X-ray bright ellipticals are believed to have global cooling inflows (e.g., Sarazin 1990). A global inflow can occur if the radiative cooling time of the gas is shorter than the age of the galaxy throughout the bulk of the optical image of the galaxy. Based on the best-fit model for the radial distribution of the soft X-ray emission, the central gas electron number density is about $n_e = 8.8 \times 10^{-3}$ cm⁻³. The central cooling time in the gas is about 4×10^8 yr, which is much shorter than the likely age of the galaxy.

The total X-ray luminosity of the gas may be too low to be consistent with a global cooling inflow involving the total stellar mass loss rate of the galaxy. The total bolometric luminosity of the gas is $L_{\text{bol}} \approx 3.6 \times 10^{40}$ ergs s⁻¹, assuming the best-fit soft component model for the unresolved emission (Table 4). Given its optical luminosity and assuming a normal elliptical galaxy stellar mass loss rate,

the total rate of stellar mass loss is about $0.5 M_{\odot} \text{ yr}^{-1}$ (e.g., Sarazin 1990). The heat input to the gas that is just associated with the motions of the gas-losing stars is $3\sigma^2/2$ per unit mass, which leads to a total heating rate of $\dot{E}_{\text{heat}} \geq 1.3 \times 10^{40}$ ergs s⁻¹. If the gas is involved in a cooling inflow, then infall in the galactic potential and adiabatic compression increase the heating rate by a factor of ~ 3 . Type Ia supernovae could also increase the heating rate by at least as large a factor. Thus, for a global cooling inflow one would expect a bolometric luminosity of $\gtrsim 8 \times 10^{40}$ ergs s⁻¹. At best, this would be marginally allowed by the observed luminosity.

However, if the gas were involved in a global cooling flow, one would expect the gas X-ray surface brightness to be much more centrally peaked than is observed (Fig. 7). In global cooling flow models, the X-ray surface brightness is generally at least as centrally peaked as the optical surface brightness (e.g., Sarazin & White 1988; Sarazin & Ashe 1989). Thus, a global cooling flow seems unlikely. On the other hand, if the interstellar gas were in a global supersonic outflow or wind, the expected X-ray luminosity ($\lesssim 10^{39}$ ergs s⁻¹) would be much smaller than is observed (D'Ercole et al. 1989).

Pellegrini & Fabbiano (1994) suggest that the gas in NGC 4697 is in a partial wind, with a cooling inflow at the center and an outflow in the outer regions. This could explain the low luminosity and gas mass in this galaxy. On the other hand, in these models the X-ray surface brightness of the gas is always more centrally condensed than the optical surface brightness (Pellegrini & Ciotti 1998), which is exactly the opposite of what we observe in NGC 4697 (Fig. 7).

Among simple spherical hydrodynamical models of isolated galaxies, the only models that seem consistent with the low X-ray luminosity, low temperature, short cooling time, and broad distribution of the gas in NGC 4697 would seem to be subsonic inflation models prior to cooling inflow (Ciotti et al. 1991; David et al. 1991). However, these models would probably require that much of the gas in the galaxy has been removed $\lesssim 10^9$ yr ago to explain the low mass of interstellar gas today and also why this galaxy is at such an early hydrodynamical stage when it appears to have a very old stellar population.

Pellegrini (1994) suggested that S0 galaxies and other rapidly rotating early-type galaxies might be more susceptible to winds and other outflows as a result of rotation. She showed that there was an apparent anticorrelation between the X-ray-to-optical ratio of early-type galaxies and their fractional rotational support. NGC 4697 might be an example of the effects of rapid rotation; this could help to explain the low mass of ISM gas. On the other hand, in this model one might expect the soft X-ray image to be highly elongated in the same direction as the optical image, which does not really seem to be the case (Fig. 2).

Alternatively, it may be that the gas in NGC 4697 has been strongly affected by ram pressure or other hydrodynamical effects of its environment (e.g., White & Sarazin 1991). The extended morphology of the gas and its distorted morphology would suggest motion of the galaxy to the northwest relative to the ambient intergalactic medium. If the motion also has a significant component along the line of sight, ram pressure might explain both the extended distribution and the distorted morphology. Of course, ram pressure stripping would also explain the low X-ray luminosity and low gas mass.

The best-fit abundance for the gas in NGC 4697 is rather low (0.06 solar) but is very poorly determined since much of the soft X-ray emission is due to lines. In any case, the abundance is consistent with the abundance-temperature correlation found by Davis & White (1996).

7.3.4. Relation to Cooler Interstellar Medium

NGC 4697 contains a small dust lane near its center (Goudfrooij et al. 1994; van Dokkum & Franx 1995), which is most prominent in images with the *HST* (e.g., Dejonghe et al. 1996). The dust lane is fairly regular and appears to be part of a disk of material that is elongated along the optical major axis of the galaxy. There is no obvious corresponding feature in the X-ray image (Fig. 1; see also Fig. 2 in Paper I).

NGC 4697 also contains an arc-shaped region of H α emission, mainly extending to the northeast of the galaxy center (Goudfrooij et al. 1994). Again, there is nothing that obviously corresponds to this in the X-ray image (Fig. 1; see also Fig. 2 in Paper I). There does appear to be a bit more diffuse emission and more sources on this side of the galaxy, but this is not a very strong effect. The spatial decomposition of the unresolved emission suggests that it is dominated by unresolved LMXBs in the central parts of the galaxy. Thus, there may be too little hot gas to interact with the cooler ISM, and/or any spatial features due to interaction of diffuse X-ray gas with cooler ISM may be washed out by emission by unresolved LMXB emission.

If the columns of cooler gas are significant, one might expect to see absorption features in the X-ray image corresponding to locations of cooler ISM. The lack of such features suggests that the columns of cooler gas are not very large ($\lesssim 6 \times 10^{20} \text{ cm}^{-2}$).

8. CONCLUSIONS

The origin of the X-ray emission in X-ray faint elliptical galaxies has been a mystery. Unlike X-ray bright early-type galaxies where the emission is dominated by interstellar gas with $kT \approx 1 \text{ keV}$, X-ray faint galaxies have both very hard ($\sim 5 \text{ keV}$) and very soft ($\sim 0.2 \text{ keV}$) spectral components. The hard component was thought to be due to LMXBs or an AGN. The origin of the very soft component was very uncertain; LMXBs (Irwin & Sarazin 1998a, 1998b), cool interstellar gas (Pellegrini & Fabbiano 1994), or faint stellar sources, such as M stars and RS CVn binaries (e.g., Pellegrini 1994), have all been suggested.

Our high spatial resolution *Chandra* observation of the X-ray faint elliptical galaxy NGC 4697 resolves most of the X-ray counts (61% within one effective radius) into point sources. A total of 90 individual sources are detected, of which ~ 80 are LMXBs associated with NGC 4697. Much of the emission is resolved even in the softest band. The dominance of LMXBs implies that this and other X-ray faint ellipticals have lost much of their interstellar gas.

On the other hand, NGC 4697 does have a modest amount of X-ray emission by hot interstellar gas. Of the unresolved emission, it is likely that about half is from fainter LMXBs, while about 23% of the total count rate is due to interstellar gas with $kT = 0.29 \text{ keV}$. The X-ray spectrum of the soft diffuse emission is fitted by a thermal model and shows clear evidence for soft X-ray lines characteristic of low-density, optically thin gas. The faint, diffuse soft X-ray emission in the *Chandra* image is very extended, indicating that the ISM gas distribution is much more extended and less centrally peaked than that of the optical light. The

spatial distribution of the gas is rounder than that of the optical light and has a somewhat irregular, L-shaped form. This may indicate that the gas has been affected by ram pressure from motions through intergalactic gas.

The X-ray luminosity and spatial distribution of the interstellar gas in NGC 4697 are inconsistent with a global spherical supersonic wind, partial wind, or global cooling flow. The gas may be undergoing subsonic inflation or a rotationally induced outflux or may be affected by ram pressure from intergalactic gas. There is no apparent relation between the X-ray-emitting interstellar gas and the dust disk or H α emission regions near the center of the galaxy.

X-ray spectral analysis of the resolved and diffuse emission indicates that the interstellar gas is the source of the very soft spectral component seen with *ROSAT* in the spectra of this and other X-ray faint early-type galaxies. Although the LMXBs produce a large amount of soft X-ray emission and some of them (the supersoft sources) do have a strong soft X-ray spectral component, taken together the spectrum of the LMXBs does not show a significant soft component. The cumulative LMXB spectrum is well fitted by thermal bremsstrahlung at $kT = 8.1 \text{ keV}$. The soft component in the spectrum is produced mainly by interstellar gas.

NGC 4697 has an X-ray source located within $1''$ of the optical center with an X-ray luminosity of $L_X = 8 \times 10^{38} \text{ ergs s}^{-1}$ (0.3–10 keV). This source may be due to an AGN and/or one or more LMXBs. Stellar dynamical measurements indicate that NGC 4697 has a massive central BH; the central X-ray luminosity implies that this BH is emitting at $\leq 4 \times 10^{-8}$ of its Eddington luminosity.

Three of the resolved sources are supersoft sources (e.g., Kahabka & van den Heuvel 1997). These are among the most distant and luminous supersoft sources known.

Seven of the resolved sources in the outer parts of NGC 4697 (about 20%) are coincident with candidate globular clusters. This implies that globular clusters are a very favorable environment to form LMXBs; the same result is true of our Galaxy (e.g., Hertz & Grindlay 1983). We discuss the possibility that all of the LMXBs in NGC 4697 (and other old stellar systems) were formed in globular clusters. An *HST* observation is needed to determine the globular cluster population of the inner regions of NGC 4697 where most of the LMXBs are located.

The X-ray-to-optical luminosity ratio for the LMXBs in NGC 4697 is $L_X(\text{LMXB}, 0.3\text{--}10 \text{ keV})/L_B = 8.1 \times 10^{29} \text{ ergs s}^{-1} L_{B\odot}^{-1}$. This is about 35% higher than the value for the bulge of M31 and about 13% higher than the value we found for the S0 galaxy NGC 1553. This suggests that there are variations in the X-ray-to-optical ratios of early-type galaxies and spiral bulges. Since much of the X-ray luminosity in NGC 4697 comes from a small number (~ 15) of bright sources, part of this variation may be due to statistical fluctuations in the number of bright sources or temporal variations in their individual emission. If most LMXBs are formed in globular clusters, then their number may correlate more directly with the population of globulars. On the other hand, in the range they have in common, the luminosity function of the bulge of M31 declines more rapidly with increasing luminosity than in NGC 4697. This suggests that the populations of LMXBs cannot simply be scaled from galaxy to galaxy.

The X-ray luminosities (0.3–10 keV) of the resolved

LMXBs range from $\sim 5 \times 10^{37}$ to $\sim 2.5 \times 10^{39}$ ergs s^{-1} . The luminosity function has a “knee” at 3.2×10^{38} ergs s^{-1} , which is approximately the Eddington luminosity of a $1.4 M_{\odot}$ NS. Based on other observations with *Chandra*, this knee appears to be a characteristic feature of the luminosity functions of LMXBs in early-type galaxies. This knee might provide a standard candle that could be used to determine distances to galaxies. This knee may separate accreting NS and BH binaries. If the brightest sources in NGC 4697 are Eddington limited, they must contain fairly massive BHs.

These and other *Chandra* observations of luminous elliptical galaxies may represent the first direct detections of NSs and stellar mass BHs in these galaxies. Our detection of a large population of binaries with NSs and massive BHs provides perhaps the most direct evidence that this elliptical galaxy (or its progenitors) once contained a large number of massive main-sequence stars. The population of LMXBs provides a tool to study the high-mass end of the initial mass function of early-type galaxies, long after the massive main-sequence stars have died.

We thank Maxim Markevitch for several extremely helpful communications concerning the background in the ACIS detector and the readout artifact and for very kindly making his blank-sky background files and software avail-

able to us. We are very grateful to Alexey Vikhlinin for providing his software package for extracting X-ray spectra and constructing the response files for extended sources. We also thank Keith Arnaud for advise on extracting spectra from *Chandra*. We are grateful to J. J. Kavelaars for providing his unpublished list of globular clusters in NGC 4697. Bill Harris, J. J. Kavelaars, and Arunav Kundu also gave helpful comments on the globular cluster population of NGC 4697. We are particularly grateful to Chris Mullis, who took an optical spectrum of the counterpart of source 72 and showed that it was a background AGN, rather than a globular cluster. We thank Shri Kulkarni for the interesting suggestion that all or most LMXBs are formed in globular clusters. Other useful suggestions were made by Bob O’Connell, Bob Rood, and Ray White, III. We thank Richard Mushotzky and Lorella Angelini for discussions of their *Chandra* results on X-ray bright ellipticals. Support for this work was provided by the National Aeronautics and Space Administration through *Chandra* awards GO0-1019X, GO0-1141X, and GO0-1173X, issued by the *Chandra X-Ray Observatory* Center, which is operated by the Smithsonian Astrophysical Observatory for and on behalf of NASA under contract NAS8-39073. J. A. I. was supported by *Chandra* Fellowship grant PF9-10009, awarded through the *Chandra* Science Center.

REFERENCES

- Allen, S. W., di Matteo, T., & Fabian, A. C. 2000, MNRAS, 311, 493
 Birkinshaw, M., & Davies, R. L. 1985, ApJ, 291, 32
 Blanton, E. L., Sarazin, C. L., & Irwin, J. A. 2001, ApJ, 552, 106
 Borozdin, K. N., & Priedhorsky, W. C. 2000, ApJ, 542, L13
 Brandt, W. N., et al. 2000, AJ, 119, 2349
 Brown, B. A., & Bregman, J. N. 1998, ApJ, 495, L75
 Canizares, C. R., Fabbiano, G., & Trinchieri, G. 1987, ApJ, 312, 503
 Ciotti, L., Pellegrini, S., Renzini, A., & D’Ercole, A. 1991, ApJ, 376, 380
 David, L. P., Forman, W., & Jones, C. 1991, ApJ, 369, 121
 Davis, D. S., & White, R. E., III 1996, ApJ, 470, L35
 Dejonghe, H., de Bruyne, V., Vauterin, P., & Zeilinger, W. W. 1996, A&A, 306, 363
 D’Ercole, A., Renzini, A., Ciotti, L., & Pellegrini, S. 1989, ApJ, 341, L9
 Fabbiano, G., Kim, D.-W., & Trinchieri, G. 1992, ApJS, 80, 531
 ———, 1994, ApJ, 429, 94
 Faber, S. M., Wegner, G., Burstein, D., Davies, R. L., Dressler, A., Lynden-Bell, D., & Terlevich, R. J. 1989, ApJS, 69, 763
 Forman, W., Jones, C., & Tucker, W. C. 1985, ApJ, 293, 102
 Garcia, M. R., Murray, S. S., Primini, F. A., Forman, W. R., McClintock, J. E., & Jones, C. 2000, ApJ, 537, L23
 Gebhardt, K., et al. 2000, ApJ, 539, L13
 Giacconi, R., et al. 2001, ApJ, 551, 624
 Goudfrooij, P., Hansen, L., Jorgensen, H. E., & Norgaard-Nielsen, H. U. 1994, A&AS, 105, 341
 Hanes, D. A. 1977, MmRAS, 84, 45
 Harris, W. E. 1991, ARA&A, 29, 543
 Hertz, P., & Grindlay, J. E. 1983, ApJ, 275, 105
 Irwin, J. A., & Bregman, J. N. 1999, ApJ, 527, 125
 Irwin, J. A., & Sarazin, C. L. 1998a, ApJ, 494, L33
 ———, 1998b, ApJ, 499, 650
 Irwin, J. A., Sarazin, C. L., & Bregman, J. N. 2000, ApJ, 544, 293 (ISB00)
 Jedrzejewski, R. I., Davies, R. L., & Illingworth, G. D. 1987, AJ, 94, 1508
 Kahabka, P., & van den Heuvel, E. P. J. 1997, ARA&A, 35, 69
 Kim, D.-W., Fabbiano, G., Matsumoto, H., Koyama, K., & Trinchieri, G. 1996, ApJ, 468, 175
 Loewenstein, M., & Mathews, W. G. 1987, ApJ, 319, 614
 Margon, B., & Ostriker, J. P. 1973, ApJ, 186, 91
 Markevitch, M. 2000, ACIS Background
 Markevitch, M., et al. 2000, ApJ, 541, 542
 Matsumoto, H., Koyama, K., Awaki, H., Tsuru, T., Loewenstein, M., & Matsushita, K. 1997, ApJ, 482, 133
 Monet, D., et al. 1998, USNO-A2.0, A Catalog of Astrometric Standards (Flagstaff: US Naval Observatory)
 Mushotzky, R. F., Cowie, L. L., Barger, A. J., & Arnaud, K. A. 2000, Nature, 404, 459
 Peletier, R. F., Davies, R. L., Illingworth, G. D., Davis, L. E., & Cawson, M. 1990, AJ, 100, 1091
 Pellegrini, S. 1994, A&A, 292, 395
 Pellegrini, S., & Ciotti, L. 1998, A&A, 333, 433
 Pellegrini, S., & Fabbiano, G. 1994, ApJ, 429, 105
 Primini, F. A., Forman, W., & Jones, C. 1993, ApJ, 410, 615
 Sarazin, C. L. 1990, In The Interstellar Medium of External Galaxies, ed. H. A. Thronson, Jr. & J. M. Shull (Dordrecht: Kluwer), 201
 Sarazin, C. L., & Ashe, G. A. 1989, ApJ, 345, 22
 Sarazin, C. L., Irwin, J. A., & Bregman, J. N. 2000, ApJ, 544, L101 (Paper I)
 Sarazin, C. L., & White, R. E., III, 1988, ApJ, 331, 102
 Shirey, R., et al. 2001, A&A, 365, L195
 Snowden, S. L., et al. 1997, ApJ, 485, 125
 Stark, A. A., Gammie, C. F., Wilson, R. W., Bally, J., Linke, R. A., Heiles, C., & Hurwitz, M. 1992, ApJS, 79, 77
 Supper, R., Hasinger, G., Pietsch, W., Trümper, J., Jain, A., Magnier, E. A., Lewin, W. H. G., & van Paradijs, J. 1997, A&A, 317, 328
 Tonry, J. L., Dressler, A., Blakeslee, J. P., Ajhar, E. A., Fletcher, A. B., Luppino, G. A., Metzger, M. R., & Moore, C. B. 2001, ApJ, 546, 681
 Trinchieri, G., Fabbiano, G., & Canizares, C. R. 1986, ApJ, 310, 637
 van Dokkum, P. G., & Franx, M. 1995, AJ, 110, 2027
 van Paradijs, J. 1978, Nature, 274, 650
 Vikhlinin, A., Markevitch, M., & Murray, S. S. 2001, ApJ, 551, 160
 Walterbos, R. A. M., & Kennicutt, R. C., Jr. 1988, A&A, 198, 61
 Wegner, G., Colless, M., Baggby, G., Davies, R. L., Bertschinger, E., Burstein, D., McMahan, R. K., & Saglia, R. K. 1996, ApJS, 106, 1
 White, N. E., Nagase, F., & Parmar, A. N. 1995, in X-Ray Binaries, ed. W. Lewin, J. van Paradijs, & E. van den Heuvel (Cambridge: Cambridge Univ. Press), 1
 White, R. E., III, & Davis, D. S. 1997, in ASP Conf. Ser. 115, Galactic Cluster Cooling Flows, ed. N. Soker (San Francisco: ASP), 217
 White, R. E., III, & Sarazin, C. L. 1991, ApJ, 367, 476